OPEN ACCESS

Electrochemical Pressure Impedance Spectroscopy for Polymer Electrolyte Membrane Fuel Cells: Signal Interpretation

To cite this article: Lutz Schiffer and Wolfgang G. Bessler 2023 *J. Electrochem. Soc.* **170** 054514

Journal of The Electrochemical Society, 2023 **170** 054514

Electrochemical Pressure Impedance Spectroscopy for Polymer Electrolyte Membrane Fuel Cells: Signal Interpretation

Lutz Schiffer and Wolfgang G. Bessler[z,*]

Institute of Sustainable Energy Systems (INES), Offenburg University of Applied Sciences, 77652 Offenburg, Germany

Electrochemical pressure impedance spectroscopy (EPIS) is an emerging tool for the diagnosis of polymer electrolyte membrane fuel cells (PEMFC). It is based on analyzing the frequency response of the cell voltage with respect to an excitation of the gas-phase pressure. Several experimental studies in the past decade have shown the complexity of EPIS signals, and so far there is no agreement on the interpretation of EPIS features. The present study contributes to shed light into the physicochemical origin of EPIS features, by using a combination of pseudo-two-dimensional modeling and analytical interpretation. Using static simulations, the contributions of cathode equilibrium potential, cathode overpotential, and membrane resistance on the quasi-static EPIS response are quantified. Using model reduction, the EPIS responses of individual dynamic processes are predicted and compared to the response of the full model. We show that the EPIS signal of the PEMFC studied here is dominated by the humidifier. The signal is further analyzed by using transfer functions between various internal cell states and the outlet pressure excitation. We show that the EPIS response of the humidifier is caused by an oscillating oxygen molar fraction due to an oscillating mass flow rate.
 [DOI: 10.1149/1945-7111/acd4ea]

Manuscript submitted January 27, 2023; revised manuscript received April 4, 2023. Published June 6, 2023.

Fuel cells are clean energy converters that convert the chemical energy stored in hydrogen to electricity and heat. If the hydrogen is generated from renewable electricity, fuel cells can contribute to solve the problem of spatially and temporally limited availability of renewable energy sources.[1,2] The most established type of fuel cell is the polymer electrolyte membrane fuel cell (PEMFC).[3] The electrochemistry of the PEMFC is complex due to the diversity of mass transport processes combined with electrochemical reactions. To optimize fuel cell performance, whether in terms of efficiency, design, or prevention of faulty operation, it is useful to deconvolute the overall cell performance into the contributions of the various transport and chemistry processes. A widely-used technique to characterize the dynamics of electrochemical systems and their underlying processes is electrochemical impedance spectroscopy (EIS). However, in the context of PEMFCs, the interpretation of the low-frequency EIS features, typically assigned to mass transport processes, remains controversial.[4] The appearance of a low-frequency arc in the Nyquist representation was often attributed to the process of diffusion in the porous electrodes.[5–7] However, Schneider et al.[8,9] explained this feature without referring to the process of diffusion. They argued that oxygen concentration oscillations extend into the gas channel and are transported downstream the channel. Their coupling with externally-imposed current oscillation causes the formation of the low-frequency arc.

To obtain additional information about mass transport processes, a modification of EIS, called electrochemical pressure impedance spectroscopy (EPIS),[10,11] has attracted the interest of researchers in the past decade. It is based on the analysis of the cell voltage response to a harmonic excitation of the cathode outlet pressure under galvanostatic control. It is obtained as the relationship between the Fourier transform of both quantities at each analyzed frequency according to

$$Z_{V/p}(\omega) = \frac{\mathcal{F}\{\Delta V_{\text{cell}}(t)\}}{\mathcal{F}\{\Delta p_{\text{CCH}}^{\text{out}}(t)\}}, \qquad [1]$$

where, the transfer function $Z_{V/p}$ is referred to as electrochemical pressure impedance (EPI) and ΔV_{cell} and $\Delta p_{\text{CCH}}^{\text{out}}$ are the differences between cell voltage and channel outlet pressure and their time-averaged values, respectively.

In 2010, Niroumand et al.[12] observed pressure-induced voltage oscillations and encouraged researchers to further investigate pressure-voltage oscillations as a diagnostic tool for PEMFCs. Several experimental studies on EPIS were recently conducted using single-cell PEMFCs. Engebretsen et al.[13] used a loudspeaker for the pressure excitation, which allowed them to measure spectra up to 100 Hz, but the spectra were subject to considerable noise. Shirsath et al.[14–18] and Zhang et al.[19] used a more accurate pressure controller for the pressure excitation, which led to a cleaner signal, albeit in a reduced frequency range below 1 Hz and 0.1 Hz, respectively. In addition to EPIS, similar new characterization methods are currently investigated which are based on the same basic idea but differ in their approach. Sorrentino et al.[20–22] excited the partial pressure of species at the cathode inlet by periodically changing specific reactant feeds and measured the electric response of the PEMFC. The spectra of this so-called concentration frequency response analysis were recorded for frequencies below 1 Hz. Kubannek and Krewer[23] recorded the response of the CO_2 flux as the product of the methanol oxidation reaction on a porous electrode during EIS and analyzed its relation to the current density, which they called species frequency response analysis.

In the case of EPIS, Shirsath et al.[14–17] and Zhang et al.[19] obtained typical common features for the operation with air as the cathode gas feed. Figure 1 shows exemplary EPI spectra in the Bode representation taken from our previous combined experimental and modeling study.[18] The figure includes numbers to indicate features of interest (FOI) of these spectra. Towards the lowest frequency of 1 mHz the magnitude converges towards a constant value (FOI 1). With increasing frequency, the magnitude increases (FOI 2) and reaches a maximum (FOI 3) around 1 Hz. In the complete frequency range of the experiments between 1 mHz–1 Hz, the phase shift decreases continuously (FOI 4) from 0° to −200°. In the extended frequency range of the simulations above 1 Hz, the magnitude shows a decrease (FOI 5) towards zero, qualitatively consistent with the experimental results of Engebretsen et al. that extended up to 100 Hz.[13]

Shirsath et al.[14] attributed the large magnitude (FOI 3) and the strongly negative phase shifts (FOI 4) to the diffusion of oxygen. This hypothesis was based on their EPIS experiments with a change of the cathode gas feed composition from air to pure oxygen,[16] for which the increase of magnitude and decrease of phase shift with frequency was less pronounced. Furthermore, they measured a strong increase of the maximum magnitude for a decrease of the oxygen stoichiometry, which they interpreted as

*Electrochemical Society Member.
[z]E-mail: wolfgang.bessler@hs-offenburg.de

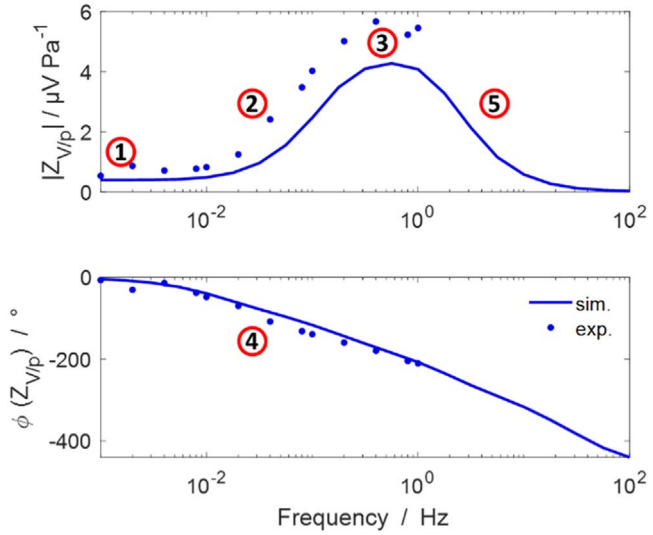

Figure 1. Simulated and experimental EPIS spectra $Z_{V/p}$ of a 100 cm^2 PEMFC operated at 55 °C on pure hydrogen (dry, $\lambda_{H_2} = 1.2$)and humidified air (55% RH, $\lambda_{O_2} = 2.5$) at 0.2 A cm^{-2}. The transfer function is shown in the Bode representation, with the magnitude $|Z_{V/p}|$ in the upper panel and the phase shift $\phi(Z_{V/p})$in the lower panel, both as function of logarithmic frequency. The data are taken from Schiffer et al.[18] Typical features of interest (FOI) are numbered in red circles.

oxygen diffusion becoming rate-controlling for a higher oxygen depletion.[14] The same trend for a variation of oxygen stoichiometry was observed by Zhang et al.,[19] who attributed the increase of the magnitude to the decrease of the oxygen concentration and hence an increase of the "mass transport impedance." Furthermore, Shirsath et al. measured an increase of the maximum magnitude for the cell operation under flooding conditions[15] and for the replacement of the gas diffusion layer (GDL) from a product with microporous layer (MPL) to one without.[14] Both trends were interpreted as hindrance of oxygen diffusion by the accumulation of liquid water close to the catalytic sites.

Although the experiments indicated that the peak value of the magnitude (FOI 3) is influenced by diffusion processes, the reason for the increase of magnitude itself (FOI 2) as well as the decrease of phase shift (FOI 4) has not yet been explained. This is, however, required for understanding the experimentally-observed relation between the maximum magnitude and the oxygen diffusion. Therefore, it is necessary to find an explanation for these observations on the base of a causal link between the outlet pressure excitation and the cell voltage response. In our previous publication,[18] we observed that the gas humidifier has a strong influence on EPIS and that the cell voltage response is closely related to the oxygen partial pressure response, which gets amplified with increasing frequency. These aspects will be further investigated here.

The aim of the present article is to deepen the understanding of EPIS. To achieve this goal, we use the pseudo-two-dimensional (P2D) model developed, parameterized and validated in our previous study.[18] We first analyze the static pressure-voltage response of the fuel cell. Second, we show the separate influence of time-dependent processes on the EPIS signal by simulating reduced model configurations. In the third part of the article, we determine the origin of the oxygen partial pressure response by relating it to the observed phenomenon of an oscillating inlet flow rate.[16] The combined investigations allow a physics-based interpretation of the FOI 1–5, which is summarized at the end of the article.

Methodology

PEMFC model.—The PEMFC model used in the present study was described in detail previously.[18] It is a P2D model which couples the dimension in through-plane direction (here: y direction) of the membrane electrode assembly (MEA) to the dimension along the gas channel (here: x direction). The dimension along the gas channel is crucial to reproduce the EPIS spectra, as the pressure propagation along the gas channel was observed to change with the excitation frequency.[16–19] A particular model feature introduced in Ref. 18 is the gas volume in the air humidifier upstream the fuel cell, which has a strong influence on the pressure dynamics and the inlet flow rate during pressure excitation.[16–18] In the following, this model is also referred to as "full model," as opposed to "reduced models" also investigated below.

The model was parametrized to and validated against experimental data of a single 100 cm^2 PEMFC (UBzM, Germany), which was described in detail by Shirsath et al.[14–17] The flow fields contain 23 serpentine channels through which the gases were passed in counterflow mode. Sigracet 29 BCE was used as GDL with 5% PTFE treatment and an MPL and Nafion™ 212 as membrane. The catalyst layers (CL) were loaded with 0.4 mg cm^{-2} platinum. The humidifier had a gas volume of 850 ml.

A summary of all model equations and parameters as well as a schematic sketch of the modeling domain are given in the Appendix.

Analytical derivative of the cell voltage with respect to pressure.—In order to understand how the cell voltage of the model changes with cathode outlet pressure, an analytical derivation based on the model equations (see Appendix) is presented in this section. In the remainder of this article the interpretation of the simulated cell voltage response will be occasionally supported by the use of the derivatives presented here.

The measured cell voltage is the potential difference between both electrodes, reduced by the ohmic losses due to the contact resistances. It is a property of the overall system and therefore spatially independent. However, the potential profile between both electrodes is dependent on local states and changes in x direction (along the channel). The derivative of the cell voltage V_{cell} with respect to cathode channel outlet pressure p_{CCH}^{out} can be approximated by the sum of the derivatives of local potential differences according to

$$\frac{\partial V_{cell}}{\partial p_{CCH}^{out}} = \frac{\partial \Delta\phi_C^{eq}(x)}{\partial p_{CCH}^{out}} + \frac{\partial \eta_C(x)}{\partial p_{CCH}^{out}} + \frac{\partial \Delta\phi_{elyt}(x)}{\partial p_{CCH}^{out}}. \quad [2]$$

Please refer to the List of Symbols (Appendix, Table A·IV) for a definition of all symbols used in the present article. At stationary conditions, $\partial V_{cell}/\partial p_{CCH}^{out}$ corresponds to the low-frequency limit of EPIS. From this equation, we see that the change of the cell voltage with cathode outlet pressure is composed of changes in the cathode equilibrium potential $\Delta\phi_C^{eq}(x)$, the cathode overpotential $\eta_C(x)$, and the electrolyte potential drop $\Delta\phi_{elyt}(x)$, all of which depend on the position x along the channel. The change of potential difference at the anode with the cathode outlet pressure is assumed to be insignificant and therefore not included in Eq. 2, supported by our simulations which show values in the order of nV Pa^{-1}. Subsequently, the terms of the right-hand side of Eq. 2 are presented separately.

Cathode equilibrium potential.—The equilibrium potential difference of the oxygen reduction reaction (ORR) at the cathode is described by the Nernst equation (cf., Appendix, Table A·I),

$$\Delta\phi_{ORR}^{eq} = -\frac{\Delta H_{ORR} - T\Delta S_{ORR}}{2F} + \frac{RT}{4F}\ln\left(\frac{p_{O_2}}{p_{ref}}\right). \quad [3]$$

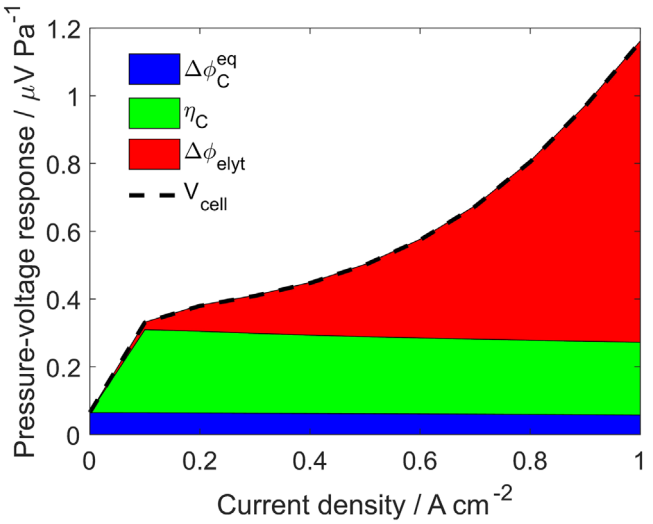

Figure 2. Simulated static pressure-voltage response (dashed line) of the PEMFC plotted as function of current density. The total response is composed of three contributions, the response of the cathode equilibrium potential (blue area), the cathode overpotential (green area) and the electrolyte potential drop (red area).

Differentiation with respect to the cathode outlet pressure leads to

$$\frac{\partial \Delta\phi_{\mathrm{C}}^{\mathrm{eq}}(x)}{\partial p_{\mathrm{CCH}}^{\mathrm{out}}} = \frac{RT}{4F}\frac{1}{p_{\mathrm{O_2,CCL}}(x)}\frac{\partial p_{\mathrm{O_2,CCL}}(x)}{\partial p_{\mathrm{CCH}}^{\mathrm{out}}}. \quad [4]$$

From this equation we can see that the equilibrium potential changes with the outlet pressure because of a change of the local oxygen pressure in the cathode catalyst layer (CCL) $p_{\mathrm{O_2,CCL}}(x)$ with the outlet pressure $(\partial p_{\mathrm{O_2,CCL}}(x)/\partial p_{\mathrm{CCH}}^{\mathrm{out}})$. It is furthermore inversely proportional to the local oxygen pressure.

Cathode overpotential.—The relationship between cathode overpotential and volumetric faradaic current density $i_{\mathrm{F}}^{\mathrm{V}}$ is implicitly described by the Butler Volmer (BV) equation (cf. Appendix, Table A·I),

$$i_{\mathrm{F}}^{\mathrm{V}} = i_0^{\mathrm{V}}\left(\exp\left[\frac{\alpha_{\mathrm{A}}F}{RT}\eta\right] - \exp\left[-\frac{\alpha_{\mathrm{C}}F}{RT}\eta\right]\right). \quad [5]$$

Table I. Parameter variation to switch individual time-dependent processes "on" and "off."

Time-dependent process	Parameter	"on"	"off"
DL charge/ discharge	$C_{\mathrm{DL}}^{\mathrm{V}}$	410 F m^{-2}	0 F m^{-2}
Water uptake PEM	σ_{elyt}	$f(\lambda)$	3.4 S m^{-1}
Gas transport GDL	L_{GDL}	212.5 μm	0 μm
Gas transport gas channel	L_{CH}	0.304 m	0 m
Humidifier	V_{hum}	850 ml	0 ml

$$i_{\mathrm{F,C}}^{\mathrm{V}}(x) = \frac{i_{\mathrm{elyt}}(x)}{L_{\mathrm{CL}}} - C_{\mathrm{DL}}^{\mathrm{V}}\frac{\partial(\Delta\phi_{\mathrm{C}}(x))}{\partial t}. \quad [7]$$

Because the faradaic and DL current are both contributing to the ionic current, the volumetric faradaic current density is equal to the ionic current through the electrolyte $i_{\mathrm{elyt}}(x)$ divided by the cathode catalyst layer (CCL) thickness L_{CL}, minus the volumetric DL current. Note that, for the present analytical derivation, we assume that the CCL is not spatially resolved in the y dimension (through-plane dimension) in order to avoid additional terms related to that dimension. The full numerical model investigated further below does include a spatially-resolved CCL.

The volumetric exchange current density of the ORR is given as (cf. Appendix, Table A·III)

$$i_0^{\mathrm{V}} = i_0^{\mathrm{V}}(p_{\mathrm{ref}}, T)\left(\frac{p_{\mathrm{O_2}}}{p_{\mathrm{ref}}}\right)^{0.54}. \quad [8]$$

By inserting Eqs. 7 and 8 into 6, the following equation for the cathode overpotential is obtained:

$$\eta_{\mathrm{C}}(x) = -\frac{RT}{\alpha_{\mathrm{C}}F}\ln\left(-\frac{\frac{i_{\mathrm{elyt}}(x)}{L_{\mathrm{CL}}} - C_{\mathrm{DL}}^{\mathrm{V}}\frac{\partial(\Delta\phi_{\mathrm{C}}(x))}{\partial t}}{i_0^{\mathrm{V}}(p_{\mathrm{ref}}, T)\left(\frac{p_{\mathrm{O_2,CCL}}(x)}{p_{\mathrm{ref}}}\right)^{0.54}}\right). \quad [9]$$

The derivation of Eq. 9 with respect to the cathode outlet pressure leads to

$$\frac{\partial \eta_{\mathrm{C}}(x)}{\partial p_{\mathrm{CCH}}^{\mathrm{out}}} = \frac{RT}{\alpha_{\mathrm{C}}F}\frac{0.54}{p_{\mathrm{O_2,CCL}}(x)}\frac{\partial p_{\mathrm{O_2,CCL}}(x)}{\partial p_{\mathrm{CCH}}^{\mathrm{out}}} - \frac{RT}{\alpha_{\mathrm{C}}F}\frac{1}{i_{\mathrm{elyt}}(x) - L_{\mathrm{CL}}C_{\mathrm{DL}}^{\mathrm{V}}\frac{\partial(\Delta\phi_{\mathrm{C}}(x))}{\partial t}}\frac{\partial i_{\mathrm{elyt}}(x)}{\partial p_{\mathrm{CCH}}^{\mathrm{out}}} - \frac{RT}{\alpha_{\mathrm{C}}F}\frac{C_{\mathrm{DL}}^{\mathrm{V}}}{-\frac{i_{\mathrm{elyt}}(x)}{L_{\mathrm{CL}}} + C_{\mathrm{DL}}^{\mathrm{V}}\frac{\partial(\Delta\phi_{\mathrm{C}}(x))}{\partial t}}\frac{\partial}{\partial p_{\mathrm{CCH}}^{\mathrm{out}}}\frac{\partial(\Delta\phi_{\mathrm{C}}(x))}{\partial t}. \quad [10]$$

To develop the derivative of the cathode overpotential, we need to invert this equation. By assuming that the anodic current of the ORR can be neglected compared to the cathodic current ($\exp[\alpha_{\mathrm{A}}F\eta/(RT)] \ll \exp[-\alpha_{\mathrm{C}}F\eta/(RT)]$), the BV equation is simplified to the Tafel law, leading to the following explicit expression of the cathode overpotential,

$$\eta_{\mathrm{C}}(x) = -\frac{RT}{\alpha_{\mathrm{C}}F}\ln\left(-\frac{i_{\mathrm{F,C}}^{\mathrm{V}}(x)}{i_{0,\mathrm{C}}^{\mathrm{V}}(x)}\right). \quad [6]$$

The volumetric faradaic current density at position x can be expressed by combining the charge continuity equation with an expression for the double layer (DL) current according to (cf. Appendix, Table A·I)

The right-hand side of this equation consists of three terms, therefore the derivative of the cathode overpotential with cathode outlet pressure can be assigned to the sum of three processes. The first term represents the change of the local oxygen pressure with the outlet pressure $(\partial p_{\mathrm{O_2,CCL}}(x)/\partial p_{\mathrm{CCH}}^{\mathrm{out}})$. This expression is similar to the change of the equilibrium potential with the outlet pressure (cf. Eq. 4), and is also inversely proportional to the oxygen pressure. The change of the cathode overpotential with the oxygen pressure can be interpreted as a change of the reaction kinetics due to a change of the exchange current density with changing oxygen pressure.

The second term represents a change of the cathode overpotential due to a change of the local ionic current density $(\partial i_{\mathrm{elyt}}(x)/\partial p_{\mathrm{CCH}}^{\mathrm{out}})$. In the overall cell response (i.e., averaged over the channel length x), this term is likely small compared to the first term, because

$\int i_{\mathrm{elyt}}(x)\mathrm{d}x \sim i_{\mathrm{cell}}$ is constant for the galvanostatic operation considered here. The third term represents a change of the cathode overpotential due to a change of the cathode potential with time $(\partial(\partial\Delta\phi_{\mathrm{C}}(x)/\partial t)/\partial p_{\mathrm{CCH}}^{\mathrm{out}})$. Due to the time derivative, this term is negligible at low frequencies (quasi-static EPIS response), but dominates towards high frequencies. Both processes (second and third term) lead to a change of the local reaction rate (Faradic current density, see Eq. 7) and hence to a change of the local overpotential.

Electrolyte potential.—The potential drop across the electrolyte at the location x depends on the local ionic current density $i_{\mathrm{elyt}}(x)$, the local membrane proton conductivity $\bar{\sigma}_{\mathrm{elyt}}(x)$ and the membrane thickness L_{PEM} according to Ohm's law,

$$\Delta\phi_{\mathrm{elyt}}(x) = \frac{i_{\mathrm{elyt}}(x)}{\bar{\sigma}_{\mathrm{elyt}}(x)} L_{\mathrm{PEM}}. \qquad [11]$$

The membrane conductivity in our full numerical model increases monotonously with the water content, which in turn is a function of the position y along the membrane thickness. The analytical Eq. 11 uses an averaged (over the membrane thickness) conductivity. Water content in turn increases strictly monotonously with the water pressure of the gas phase in the adjacent catalyst layers (CLs). The relationship between the average proton conductivity and the water pressure in the CCL is complex and is approximated here through the following linearization approach:

$$\bar{\sigma}_{\mathrm{elyt}}(x) = A + B p_{\mathrm{H_2O,CCL}}(x). \qquad [12]$$

Due to the monotonous relationships between conductivity and water content, and water content and water pressure, the two coefficients A and B are positive. The linearization can be justified by the fact that EPIS is based on a small perturbation around a constant operation point. The coefficients A and B thus depend on the operation point and could be derived from the full numerical model; however, for the present analysis this is not necessary.

Inserting Eqs. 12 in 11 and differentiating with respect to the cathode outlet pressure leads to

$$\frac{\partial\Delta\phi_{\mathrm{elyt}}(x)}{\partial p_{\mathrm{CCH}}^{\mathrm{out}}} = -i_{\mathrm{elyt}}(x) L_{\mathrm{PEM}} \frac{B}{(\bar{\sigma}_{\mathrm{elyt}}(x))^2} \frac{\partial p_{\mathrm{H_2O,CCL}}(x)}{\partial p_{\mathrm{CCH}}^{\mathrm{out}}} + \left(\frac{L_{\mathrm{PEM}}}{\bar{\sigma}_{\mathrm{elyt}}(x)}\right) \frac{\partial i_{\mathrm{elyt}}(x)}{\partial p_{\mathrm{CCH}}^{\mathrm{out}}}. \qquad [13]$$

The right-hand side this equation has two terms. The first term shows that the electrolyte potential drop changes with the outlet pressure because of a change of the water pressure with the outlet pressure $(\partial p_{\mathrm{H_2O,CCL}}(x)/\partial p_{\mathrm{CCH}}^{\mathrm{out}})$. This relation is proportional to the ionic current density and inversely proportional to the square of the conductivity. Increasing current density should therefore lead to an increase of the absolute value of the pressure-voltage response, while increasing humidification (increasing $\bar{\sigma}_{\mathrm{elyt}}$) should lead to a decrease. The term shows the complex interdependence of the electrolyte-related EPIS response with current density and membrane conductivity.

The second term of Eq. 13 shows that, similar to the derivative of the overpotential (cf. Eq. 10), the change of the electrolyte potential drop is also caused by a change of the local ionic current density $(\partial i_{\mathrm{elyt}}(x)/\partial p_{\mathrm{CCH}}^{\mathrm{out}})$. As discussed above in the context of Eq. 10, this term is probably small compared to the first term because of the galvanostatic operation considered here.

EPIS simulations.—The procedure of the EPIS simulations was described in detail in our previous article[18] and is not repeated here. All EPIS simulations in this article were conducted at a cell current density of 0.2 A cm^{-2} at which we obtained the best agreement with the experiments.[18] For all simulations, the cell was operated with humidified air (55% RH) as cathode gas feed with an oxygen stoichiometry of 2.5 and with dry hydrogen (approx. 5% RH remaining) as anode gas feed with a stoichiometry of 1.2. The temperature was fixed to 55 °C and the average outlet pressure to 116 325 Pa. The static pressure-voltage response was simulated at the same conditions with the exception of the variation of the current density.

The analyzed transfer functions are defined subsequently. In EPIS, the dynamic relationship between the cell voltage response and the cathode outlet pressure excitation is analyzed under galvanostatic control. The transfer function $Z_{V/p}$ is calculated as the relationship between the Fourier transform of both quantities at each analyzed frequency according to Eq. 1.

In the later part of this paper, we will use additional transfer functions in order to support EPIS understanding. The average (along the channel) oxygen partial pressure response is analyzed by means of the transfer function

$$Z_{\bar{p}\,(\mathrm{O_2})/p}(\omega) = \frac{\mathcal{F}\{\Delta\bar{p}_{\mathrm{O_2,CCH}}(t)\}}{\mathcal{F}\{\Delta p_{\mathrm{CCH}}^{\mathrm{out}}(t)\}}. \qquad [14]$$

The average (along the channel) total pressure response is calculated by the transfer function

$$Z_{\bar{p}/p}(\omega) = \frac{\mathcal{F}\{\Delta\bar{p}_{\mathrm{CCH}}(t)\}}{\mathcal{F}\{\Delta p_{\mathrm{CCH}}^{\mathrm{out}}(t)\}}. \qquad [15]$$

To analyze the average (along the channel) oxygen molar fraction response, we use the transfer function

$$Z_{\bar{x}\,(\mathrm{O_2})/p}(\omega) = \frac{\mathcal{F}\{\Delta\bar{x}_{\mathrm{O_2,CCH}}(t)\}}{\mathcal{F}\{\Delta p_{\mathrm{CCH}}^{\mathrm{out}}(t)\}}. \qquad [16]$$

Another quantity which is analyzed in the frequency domain is the oscillation of the inlet flow rate at the cathode gas channel inlet $Q_{\mathrm{CCH}}^{\mathrm{in}}$. The corresponding transfer function is defined as

$$Z_{Q/p}(\omega) = \frac{\mathcal{F}\{\Delta Q_{\mathrm{CCH}}^{\mathrm{in}}(t)\}}{\mathcal{F}\{\Delta p_{\mathrm{CCH}}^{\mathrm{out}}(t)\}}. \qquad [17]$$

The volumetric flow rate in the enumerator is calculated in Nl s^{-1} and is therefore rather a measure of the actual mass flow than a measure of the actual volumetric flow rate.

Results and Discussion

Static pressure-voltage response.—EPIS represents the dynamic relationship between the cell voltage and the cathode outlet pressure during harmonic excitation. The low-frequency (quasi-static) limit of EPIS represents the static pressure-voltage relationship of the cell,

$$\lim_{\omega\to 0} Z_{V/p}(\omega) = \frac{\partial V_{\mathrm{cell}}}{\partial p_{\mathrm{CCH}}^{\mathrm{out}}}. \qquad [18]$$

This value is indicated as FOI 1 in Fig. 1. In order to interpret FOI 1, in this section we investigate the static pressure-voltage relationship. For this purpose, steady-state simulations with the P2D model were carried out for a reference pressure of 116 325 Pa (the outlet pressure used in the experiments) and for a pressure increase of 100 Pa, at current densities between 0–1.0 A cm^{-2}. The static pressure-voltage response was then calculated as

$$\frac{\partial V_{\mathrm{cell}}}{\partial p_{\mathrm{CCH}}^{\mathrm{out}}} \approx \frac{\Delta V_{\mathrm{cell}}}{\Delta p_{\mathrm{CCH}}^{\mathrm{out}}} = \frac{V_{\mathrm{cell}}(p_{\mathrm{CCH}}^{\mathrm{out}} = p_{\mathrm{ref}} + 100\ \mathrm{Pa}) - V_{\mathrm{cell}}(p_{\mathrm{CCH}}^{\mathrm{out}} = p_{\mathrm{ref}})}{100\ \mathrm{Pa}}. \qquad [19]$$

As discussed above (section analytical derivative of the cell voltage with respect to pressure), the overall cell voltage response can be deconvoluted into three contributions, that is, changes in cathode equilibrium potential $\Delta\phi_C^{eq}$, cathode overpotential η_C, and electrolyte potential drop $\Delta\phi_{elyt}$. The P2D model allows to access the local internal cell states and therefore to quantify these contributions.

The simulated static pressure-voltage response is shown in Fig. 2 as function of current density. The three contributions were averaged over the channel length and are stacked on top of each other in this figure. At open-circuit voltage (OCV, $i_{cell} = 0\,A\,cm^{-2}$), the cell voltage only changes due to the change of the cathode equilibrium potential, resulting in a value of $\frac{\partial V_{cell}}{\partial p_{CCH}^{out}} = 0.065\ \mu V\ Pa^{-1}$. This value can be approximated by the use of the derivative of the equilibrium potential with respect to the cathode outlet pressure given in Eq. 4. To this goal, the product of the reciprocal oxygen partial pressure and its derivative in Eq. 4 can be approximated as

$$\frac{1}{p_{O_2,CCL}(x)}\frac{\partial p_{O_2,CCL}(x)}{\partial p_{CCH}^{out}} = \frac{1}{p_{CCL}(x)}\frac{\partial p_{CCL}(x)}{\partial p_{CCH}^{out}} + \frac{1}{x_{O_2,CCL}(x)}\frac{\partial x_{O_2,CCL}(x)}{\partial p_{CCH}^{out}} \approx \frac{1}{p_{CCL}(x)}\frac{\partial p_{CCL}(x)}{\partial p_{CCH}^{out}} \approx \frac{1}{p_{CCL}(x)} \approx \frac{1}{\bar{p}_{CCL}}. \quad [20]$$

First, the oxygen partial pressure is replaced by the product of its molar fraction and the total pressure and subsequently differentiated. For a pressure increase at steady state, the change of molar fraction is insignificant, hence its derivative is assumed to be zero. Furthermore, the change of total pressure is assumed to be uniform throughout the cathode (gas channel, GDL and CL), which is reasonable at OCV. Finally, the local pressure along the channel is replaced by its average value. With these modifications, Eq. 4 becomes

$$\frac{\partial \Delta\phi_C^{eq}}{\partial p_{CCH}^{out}} = \frac{RT}{4F}\frac{1}{\bar{p}_{CCL}}. \quad [21]$$

This equation, derived from the Nernst equation, allows to calculate the quasi-static EPIS magnitude at OCV. Using the value of the simulated average pressure in the CL of $\bar{p}_{CCL} = 117\,181\,Pa$, the equation yields a value of $0.060\ \mu VPa^{-1}$, which compares well with the simulated value of the full model. As a comparison, Engebretsen et al.[13] reported a measured voltage increase of $0.15\ \mu V\ Pa^{-1}$ at OCV, which they stated to be consistent with the Nernstian response at 70 °C. However, even for a temperature of 70 °C and a reduced cathode pressure equal to the ambient pressure (lower limit of Engebretsen's experiments), the use of Eq. 21 leads to a change of the Nernst potential with pressure of only$0.073\ \mu VPa^{-1}$. The difference between the change of OCV with pressure measured by Engebretsen et al. and our theoretical value may hypothetically be explained as follows. The measured OCV normally deviates from the Nernst potential, which we also observed in our previous combined modeling and experimental analysis.[18] One possible reason for this difference is the effect of hydrogen crossover.[24] This phenomenon might depend on the cathode pressure and therefore, in addition to the Nernst potential, contribute to the cell voltage change with pressure.

When the fuel cell is operated under load (Fig. 2, $i_{cell} > 0\,A\,cm^{-2}$), the response of the equilibrium potential $\Delta\phi_C^{eq}$ (blue area) remains almost the same; it slightly decreases with increasing current density down to $0.058\ \mu V\ Pa^{-1}$ at $1.0\,A\,cm^{-2}$. This decrease can be explained by the increase of the average pressure along the channel (cf. Eq. 21). The average pressure increases with current density due to higher pressure losses along the channel for an increased flow rate under stoichiometric control. In addition, the response of the cathode overpotential η_C and electrolyte potential drop $\Delta\phi_{elyt}$ contribute to the cell voltage response. At low current densities (below ca. $0.5\,A\,cm^{-2}$), the largest contribution is from the overpotential. It changes with outlet pressure according to Eq. 10. Without considering the time-dependent terms for the present static analysis, Eq. 10 simplifies to

$$\frac{\partial \eta_C(x)}{\partial p_{CCH}^{out}} = \frac{RT}{\alpha_C F}\frac{0.54}{p_{O_2,CCL}(x)}\frac{\partial p_{O_2,CCL}(x)}{\partial p_{CCH}^{out}} + \frac{RT}{\alpha_C F}\frac{1}{-i_{elyt}(x)}\frac{\partial i_{elyt}(x)}{\partial p_{CCH}^{out}}. \quad [22]$$

The first term on the right-hand side describes the change of the cathode overpotential caused by a change of the oxygen pressure and has a similar form as for the cathode equilibrium potential (cf. Eq. 4). Using Eq. 20, it can be simplified to

$$\frac{RT}{\alpha_C F}\frac{0.54}{p_{O_2,CCL}(x)}\frac{\partial p_{O_2,CCL}(x)}{\partial p_{CCH}^{out}} \approx \frac{RT}{\alpha_C F}\frac{0.54}{\bar{p}_{CCL}}. \quad [23]$$

For $i_{cell} = 0.1\,A\,cm^{-2}$ the use of Eq. 23 yields $0.231\ \mu V\ Pa^{-1}$, which agrees well with the value predicted by the full model (Fig. 2) of $0.245\ \mu V\ Pa^{-1}$. This expression does not directly depend on current density, but will be affected by it through $\bar{p}_{CCL}$.

The derivative of the overpotential (cf. Eq. 22) contains a second term which describes the change of the cathode overpotential caused by a change of the local current density. Although the cell current density is constant for a galvanostatic operation, the current density can change locally. However, as discussed above in the context of Eq. 10, this term is small.

The influence of the electrolyte potential drop $\Delta\phi_{elyt}$ on the pressure-voltage response increases nonlinearly with increasing current density. At high current densities (above ca. $0.5\,A\,cm^{-2}$), it is the dominating contribution. The electrolyte potential drop changes with the outlet pressure according to Eq. 13. The first term shows the complex influence of current density i_{elyt}, electrolyte conductivity $\bar{\sigma}_{elyt}$ and water pressure $p_{H_2O,CCL}$, all of which are interdependent: An increase of the water pressure leads to an increased humidification and hence conductivity of the electrolyte, and an increase of current density typically leads to an increase of water pressure. These interdependencies likely causethe nonlinear behavior shown in Fig. 2. Still, the influence of current density (proportional according to Eq. 13) seems to be dominating, which is the reason why the highest share of the static pressure-voltage response at $1.0\,A\,cm^{-2}$ is the change of the electrolyte potential drop. The second term of Eq. 13 is likely to be small compared to the first one, as discussed above in the description of Eq. 13.

Influence of time-dependent fuel cell processes on EPIS.—The previous section focused on the interpretation of FOI 1 (cf. Fig. 1), the quasi-static EPIS response. The remaining FOI 2–5 occur at finite excitation frequencies and are therefore caused by time-dependent processes taking place within the fuel cell. In this section we use the P2D model to study the individual influences of the various processes included in the model on EPIS. The time-dependent processes included in the model are the charge and discharge of the electric DL, water uptake by the polymer electrolyte membrane (PEM), gas transport through the GDL, gas transport through the gas channel, and gas accumulation within the humidifier. The CL was not spatially resolved and therefore excluded in this study. The separation of the individual processes was realized by simulating different model configurations in which the process of interest was switched "on," while the other processes were switched

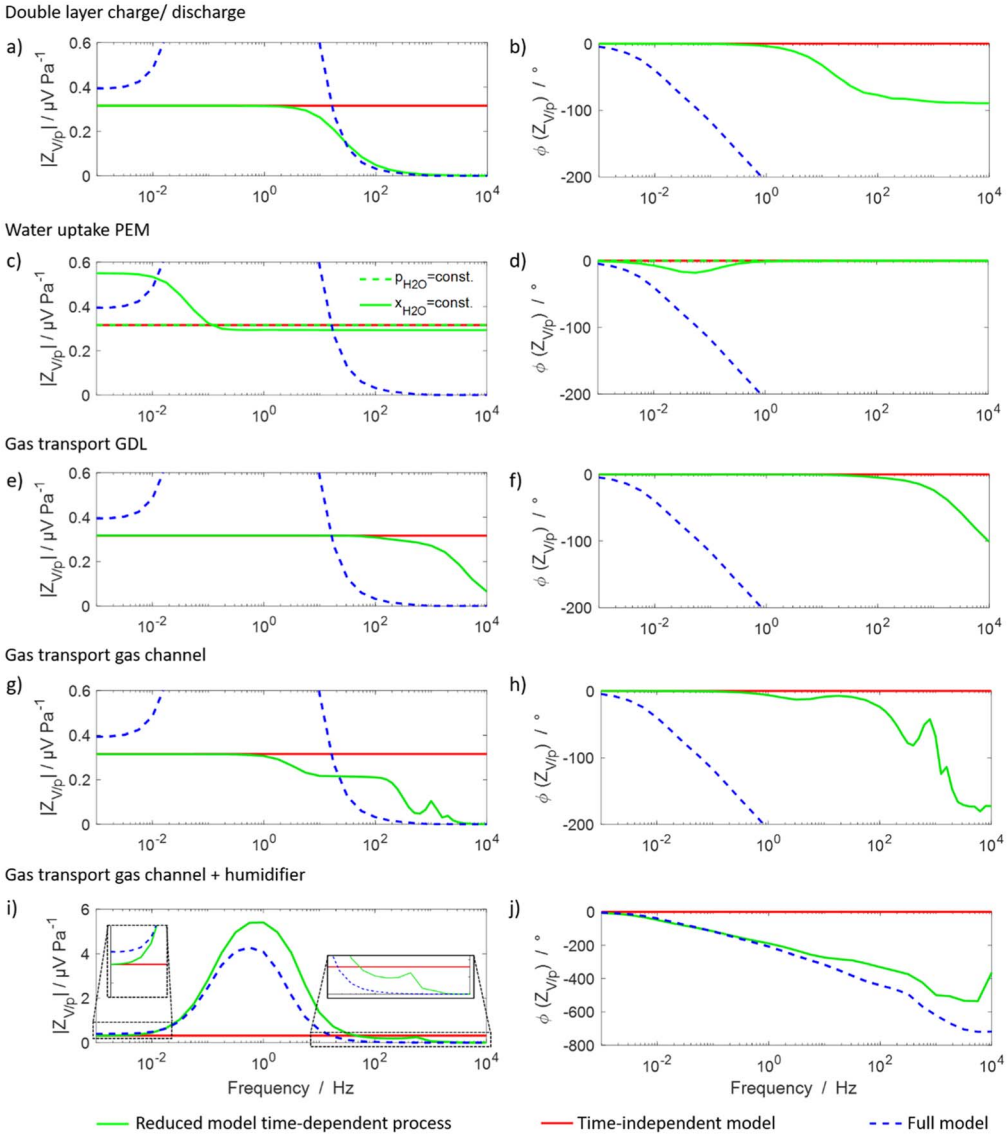

Figure 3. Simulated EPI spectra $Z_{V/p}$ at 0.2 A cm^{-2} in Bode representation (left row: magnitude, right row: phase shift) for different model configurations. Each row shows a reduced model with an individual time-dependent processes switched "on," cf. Tables Ia, Ib) Electrical double layer (DL); c), d) polymer membrane water transport; e), f) gas transport in the gas diffusion layer (GDL); g), h) gas transport in the channel; i), j) humidifier plus gas transport in the channel. All panels include the time-independent model (cf. text) and the full model (same as in Fig. 1) for comparison.

"off." The respective parameter variations are shown in Table I. All simulations were conducted at a cell current density of 0.2 A cm^{-2}, at which the best agreement between the simulations and the experiments was observed before.[18] The analyzed frequency range was extended to a maximum frequency of 10 kHz, since the features of some processes are visible only above 100 Hz. All results are shown in Fig. 3 and will be discussed in the following subsections.

Time-independent model.—For each variation, the EPIS simulation of the respective model configuration was compared to the full model and a reference model in which all time-dependent processes were switched "off." Hereafter, this configuration is called the time-independent model. Note that, with all processes switched "off," the P2D model becomes a 0D model. It is shown in all panels of Fig. 3 as red solid line. The simulated transfer function $Z_{V/p}$ of the time-independent model is a frequency-independent scalar with the value of 0.316 μV Pa^{-1}.

This value can also be derived analytically by inserting Eqs. 4, 10 and 13 into 2 with the following simplifications being valid for the time-independent model: no double-layer capacity ($C_{DL}^{V} = 0$), constant ionic current through the electrolyte due to no resolution of the model in x-direction and galvanostatic operation ($\partial i_{elyt}/\partial p = 0$), constant conductivity of the electrolyte ($B = 0$, cf. Eq. 12), all spatial variations neglected. This yields the expression

$$\frac{\partial V_{cell}}{\partial p} = \frac{RT}{F}\left(\frac{1}{4} + \frac{0.54}{\alpha_C}\right)\frac{1}{p_{O_2}}\frac{\partial p_{O_2}}{\partial p} = \frac{RT}{F}\left(\frac{1}{4} + \frac{0.54}{\alpha_C}\right)\frac{1}{p - p_{H_2O}}. \quad [24]$$

Using the parameters $p_{O_2} = x_{O_2,dry}(p - p_{H_2O})$, $x_{O_2,dry} = 0.21$, $p = 116\,325$ Pa and $p_{H_2O} = \varphi_C p_{sat}(T) = 0.55 \cdot 15\,760$ Pa $= 8668$ Pa, this equation yields a value of $\partial V_{cell}/\partial p = 0.316$ μV Pa^{-1}, consistent with the value predicted by the simulation. The change of the cell voltage with pressure in Eq. 24 (here we use the symbol p without additional subscript CCH because this 0D model considers neither gas channel nor GDL) is equal to the change of the equilibrium

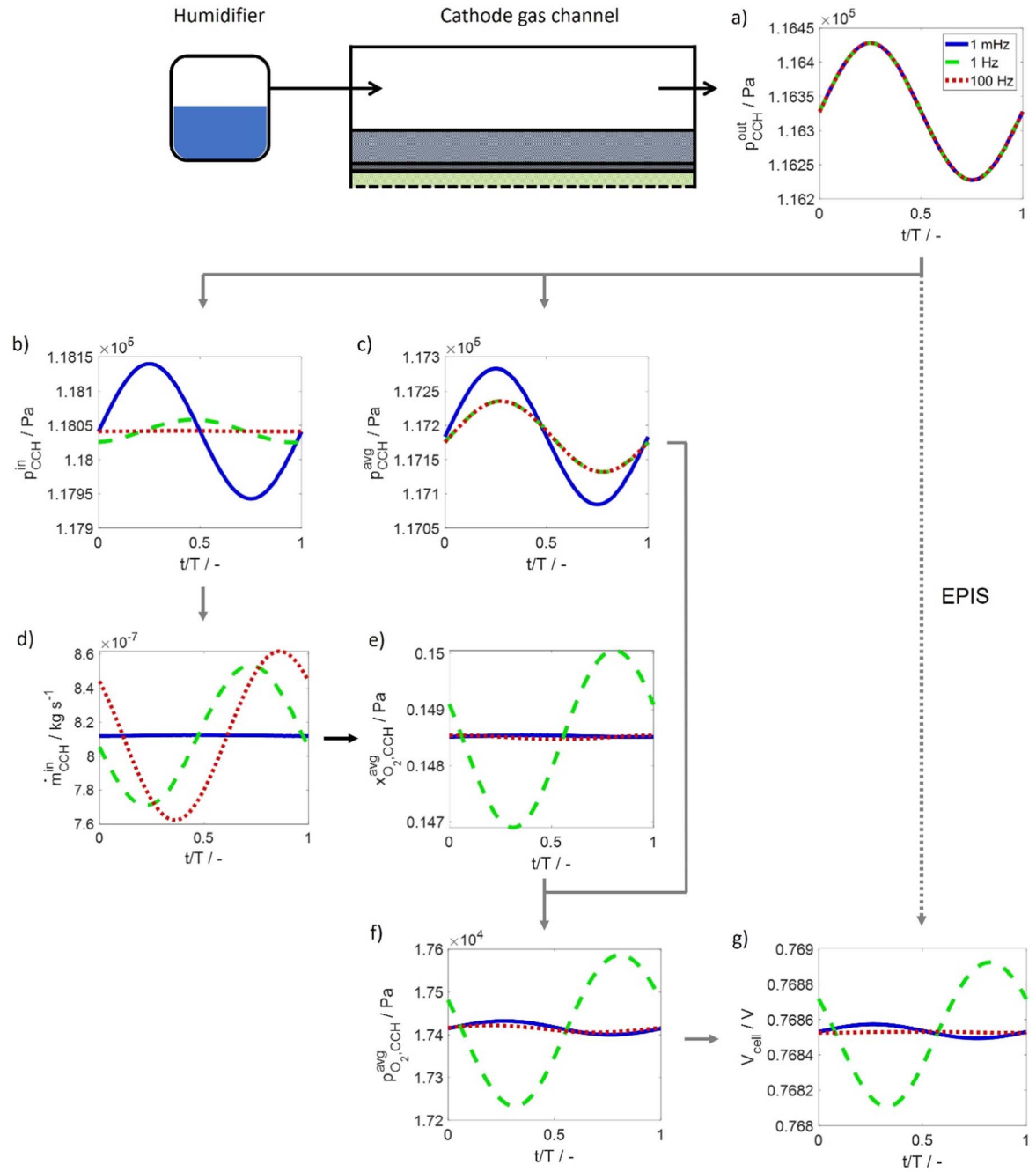

Figure 4. Time-domain behavior of internal states in the coupled fuel cell/humidifier system. Each panel shows three curves at different excitation frequencies (1 mHz, 1 Hz, 100 Hz), normalized to a common time scale. a) Outlet pressure, b) pressure at humidifier and channel inlet, c) channel-averaged pressure, d) mass flow rate at channel inlet, e) channel-averaged oxygen molar fraction, f) channel-averaged oxygen partial pressure, g) cell voltage.

potential and the change of the cathode overpotential, due to the change of oxygen pressure (Eqs. 4, 10).

Electrical double layer.—In this section, the influence of the DL charge and discharge on EPIS is analyzed. By switching "on" the DL via the parameter of the DL capacity, the model is still 0D. However, in addition to the faradaic current, now the DL current is flowing proportional to the change of the cathode Galvani potential with time (cf. Eq. 7).

Figures 3a and 3b compare simulated EPI spectra of the time-independent model and the model considering the charge and discharge of the DL. In the frequency region below 1 Hz, the magnitude and phase shift are the same for both models. The influence of the DL becomes visible above 1 Hz. The magnitude drops between 1 and 100 Hz and approaches zero for frequencies beyond. In the same frequency range, the phase shift decreases from 0° towards −90°.

To interpret the observed features caused by the DL, the derivative of the cell voltage with respect to the pressure excitation is considered again. We insert Eqs. 4, 10 and 13 into 2, this time using the following simplifications: constant ionic current through the electrolyte due to no resolution of the model in x-direction and operation under galvanostatic ($\partial i_{\mathrm{elyt}}/\partial p = 0$), constant conductivity of the electrolyte ($B = 0$, cf. Eq. 12), all spatial variations neglected. This results in the following expression for the derivative of the cell voltage with respect to the pressure excitation,

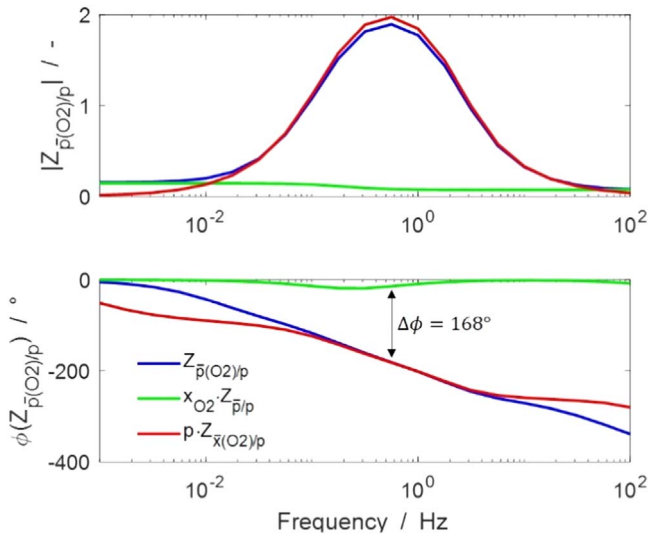

Figure 5. Simulated spectra of the transfer function $Z_{\tilde{p}(O_2)/p}$ between the average partial pressure oscillation of oxygen in the channel and the outlet pressure excitation at 0.2 A cm^{-2} in Bode representation (blue line). Additionally, the two terms of Eq. 31 are shown. The first term (green line) includes the transfer function $Z_{\tilde{p}/p}$ between the average total pressure oscillation along the channel and the outlet pressure excitation. The second term (red line) includes the transfer function $Z_{\tilde{x}(O_2)/p}$ between the average molar fraction oscillation of oxygen along the channel and the outlet pressure excitation.

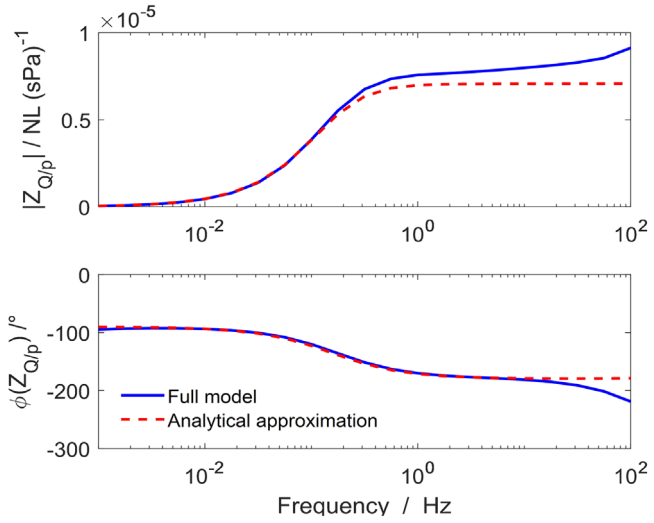

Figure 6. Spectra of the transfer function $Z_{Q/p}$ between the inlet flow rate oscillation and the outlet pressure excitation for a current density of 0.2 A cm^{-2} in Bode representation. The inlet flow rate was calculated with the analytical approximation of Eq. 34 (dashed line) and alternatively extracted from the full model simulation (solid line). The flow rate corresponds to the total of all 23 channels.

$$\frac{\partial V_{\text{cell}}}{\partial p} = \frac{RT}{F}\left(\frac{1}{4} + \frac{0.54}{\alpha_C}\right)\frac{1}{p - p_{H_2O}} - \frac{RT}{\alpha_C F} C_{DL}^{V} \frac{\frac{\partial}{\partial p}\left(\frac{\partial(\Delta\phi_C)}{\partial t}\right)}{-\frac{i_{\text{elyt}}}{L_{CL}} + C_{DL}^{V}\frac{\partial(\Delta\phi_C)}{\partial t}}. \quad [25]$$

For low frequencies and therefore slow changes of the cathode Galvani potential, $\partial(\Delta\phi_C)/\partial t \to 0$ and the last term of this equation becomes negligible. The equation is then equal to the time-independent model (cf. Eq. 24). From Fig. 3b, we see that this is the case in the frequency range below 1 Hz.

With increasing frequency, the change of the Galvani potential per time increases, which leads to an increase of the last term in the equation above. From Fig. 3a, we see that $\partial V_{\text{cell}}/\partial p$ becomes zero above ca. 1 kHz, indicating that the last term approaches the same value as the first term. More practically spoken, the increase of the Galvani potential change per time leads to an increase of the DL charge and discharge current. To keep the cell current constant at galvanostatic control, the faradaic current has to change accordingly. This in turn leads to a change of the overpotential and hence cell voltage with an opposite sign compared to the cell voltage change caused by the oxygen pressure change (cf. first term of Eq. 25).

The simulated DL EPIS feature has a characteristic frequency (frequency at minimum of imaginary part) of 18 Hz. This corresponds almost exactly to the characteristic frequency of the "classical" EIS response of 16 Hz that was simulated before using the same model.[18] Hence, it can be concluded that the electrical DL causes features both in EIS and EPIS at the same frequency.

When comparing the EPI spectrum of the full model (Figs. 3a and 3b, dashed blue line) to that of the reduced model (green solid line), the most obvious difference is the lack of the main feature (FOI 3 and 4) in the reduced model. Also, the quasi-static magnitude (towards low frequencies) shows a difference between full and reduced model. However, the final drop in magnitude around 100 Hz of the full model coincides with that of the reduced model. This allows the following interpretation: the DL is not responsible for the main FOIs 3–5, but results in a final drop of EPIS magnitude towards zero at high frequencies.

Water uptake into the PEM.—In this section, the influence of the water uptake into the PEM on EPIS is analyzed. To this end, the time-independent model was extended by a spatially resolved PEM layer, resulting in a 1D model in y dimension. The model considers the sorption of water into the electrolyte and the transport of water through the electrolyte via electro-osmotic drag and diffusion. The sorption depends on the water pressure of the adjacent gas phase, and dynamic changes of electrolyte water content get distributed through the PEM by the finite-rate transport mechanisms. The conductivity of the PEM is no longer constant, but becomes a function of water content and hence changes with pressure, too. The conductivity of the PEM, in turn, determines the electrolyte potential drop and thus the cell voltage.

In the simulations of the previous subsections, the water pressure at the cathode inlet is a boundary condition because the humidifier upstream the fuel cell provides a constant relative humidity. During pressure excitation, the water pressure therefore does not change at the cathode inlet, although it does so along the rest of the cathode. In case of the present model configuration without gas channel or GDL, the boundary condition of constant water pressure applies to the CL and therefore pressure excitation does not cause any change in cell voltage. To still work out the influence of water pressure for the present model configuration, additional simulations were carried out with the boundary condition changed from constant water pressure p_{H_2O} to constant water molar fraction $x_{H_2O} = p_{H_2O}/p$. With this, the oscillating total pressure p causes an oscillating water pressure.

Figures 3c and 3d show a comparison of simulated EPI spectra between the time-independent model and the model considering the water uptake of the PEM. In the case of constant water pressure (dashed green line), the transfer function is constant and frequency-independent, the same as for the time-independent model. In case of constant molar fraction of water (solid green line), the water pressure is oscillating proportionally to the absolute pressure and the influence of water uptake into PEM on EPIS becomes visible. The quasi-static magnitude (frequencies < ca. 10 mHz) is nearly twice the value of the time-independent model. A comparison of these values with the static pressure-voltage response of the full model at 0.2 A cm^{-2} (cf. Fig. 2b) shows that the change of the electrolyte

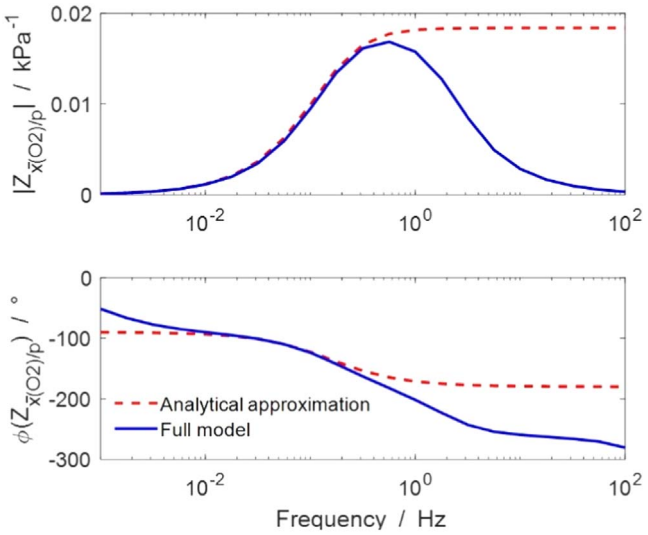

Figure 7. Spectra of the transfer function $Z_{\bar{x}(O_2)/p}$ between the average oxygen molar fraction oscillation and the outlet pressure excitation for a current density of 0.2 A cm^{-2} in Bode representation. The figure compares the analytical approximation using Eq. 45 (dashed line) to the results of the full model simulation (solid line).

potential drop with pressure for the present, reduced model is clearly larger. These observations probably originate from the difference in boundary condition.

The time dependence of the water uptake by the PEM becomes mainly visible in the frequency range between 10–100 mHz. In this frequency range, the magnitude decreases and approaches a constant value slightly below that of the time-independent model. The decrease of magnitude is accompanied by a minimum in the phase shift of −20° at around 50 mHz.

To further interpret this feature, the derivative of the cell voltage with respect to the pressure excitation is considered again by inserting Eqs. 4, 10 and 13 into 2. For the given model configuration, the following simplifications can be made: no double layer capacity ($C_{DL}^{V} = 0$); constant ionic current through the electrolyte due to no resolution of the model in x-direction and operation under galvanostatic ($\partial i_{elyt}/\partial p = 0$); spatial variations in x dimension neglected. Considering a constant water molar fraction as boundary conditions, the derivative can be simplified to

$$\frac{\partial V_{cell}}{\partial p} = \frac{RT}{F}\left(\frac{1}{4} + \frac{0.54}{\alpha_C}\right)\frac{1}{p} - \frac{i_{elyt} L_{PEM}}{\bar{\sigma}_{elyt}^2}\frac{\partial \bar{\sigma}_{elyt}}{\partial p}. \qquad [26]$$

The first term on the right-hand site is different to the expression in Eq. 24 because of the different boundary condition of constant molar fraction, which leads to a different expression for the oxygen pressure (here: $p_{O_2} = x_{O_2} p$). From the last term of Eq. 26 it can be seen that the change of the electrolyte potential drop is caused by a change of the electrolyte conductivity. The dynamics of the electrolyte conductivity is caused by the finite rate of water diffusion inside the electrolyte.

The constant magnitude in the frequency range above 1 Hz corresponds to the change of Galvani potential caused by the oxygen pressure. The magnitude is slightly below the magnitude of the time-independent model because of the change of the boundary condition. The difference can be seen by comparing Eq. 24 with the first term on the right-hand side of Eq. 26.

When comparing the EPIS spectrum of the full model to that of the reduced model (Figs. 3c and 3d, it becomes clear that the difference in the quasi-static EPIS response ($|Z_{V/p}|$ towards low frequencies: FOI 1) between full and time-independent model can be explained through the water uptake in the electrolyte: this is the only investigated model configuration that shows a difference to the time-independent model in this frequency range. The other FOI 2–5 of the full model show a qualitatively and quantitatively different behavior and are therefore not caused by water transport in the membrane.

Gas transport in the GDL.—In this section, the influence of the gas transport through the GDL on EPIS is analyzed. To this end, the time-independent model is extended by the GDL. The gas pressure and composition in the CL becomes influenced by the time-dependent process of finite-velocity transport trough the GDL. The model considers two transport mechanisms, that is, diffusion due to a concentration gradient, and convection due to a pressure gradient.

Figures 3e and 3f compare simulated EPI spectra of the time-independent model and the model considering the gas transport through the GDL. For frequencies below 100 Hz the spectra are almost the same for both model configurations, and magnitude and phase shift are superimposed. Only above 100 Hz the influence of the gas transport through the GDL becomes visible. It is important to realize that this is well above the frequency range of the experimental studies and above the maximum frequency of the simulations shown in Fig. 1. The magnitude shows a continuous decrease and has a remaining magnitude of 20% of the maximum value at 10 kHz. The phase shift shows a monotonous decrease above 100 Hz, leading to a phase shift of −100° at 10 kHz.

The derivative of the cell voltage with respect to the excitation pressure (insertion of Eqs. 4, 10 and 13 into 2) can be simplified for the given model setup, keeping in mind the extension of the GDL in y dimension. Using the assumptions, no double layer capacity ($C_{DL}^{V} = 0$), constant ionic current through the electrolyte due to no resolution of the model in x-direction and operation under galvanostatic ($\partial i_{elyt}/\partial p = 0$), constant conductivity of the electrolyte ($B = 0$, cf. Eq. 12), and ignoring gradients in x direction, the pressure derivative of the cell voltage can be written as

$$\frac{\partial V_{cell}}{\partial p_{GDL}^{y=0}} = \frac{RT}{F}\left(\frac{1}{4} + \frac{0.54}{\alpha_C}\right)\frac{1}{p_{O_2,CL}}\frac{\partial p_{O_2,CL}}{\partial p_{GDL}^{y=0}}. \qquad [27]$$

The pressure excitation is at the exterior of the GDL which is indicated by the superscript y = 0 (note that this configuration does not have a channel, therefore p_{CCH}^{out} is undefined). From this equation it can be seen that the cell voltage oscillation ∂V_{cell} follows the oxygen pressure oscillation in the CL, $\partial p_{O_2,CL}$. Therefore, the decrease in magnitude and phase shift above 100 Hz has to be caused by a decrease and delay of the average oxygen pressure oscillation in the CL caused by finite-rate transport through the GDL.

Our model includes two transport mechanisms in the GDL, diffusion and convection. We believe that the observed feature is not due to diffusion for the following reason. The time scale (here: ca. 1 kHz) is considerably higher than what is considered in literature as diffusion time scale. For example, Ziegler et al.[25] estimated the time constant for a typical GDL thickness of 300 μm, which is comparable to 212.5 μm of the present cell. They reported that oxygen gradients through the GDL reach equilibrium within 0.05 s (which corresponds to a characteristic frequency of 20 Hz). Therefore, diffusion processes are not dominantly affected by pressure excitation. Hence, we postulate that the observed EPIS feature of this specific model configuration is caused by convection instead of diffusion.

When comparing the spectra of the full and reduced models (Figs. 3e and 3f, it becomes clear that none of the observed FOI of the full model can be interpreted as gas transport in the GDL.

Gas transport in the gas channel.—In this section the influence of the gas transport through the gas channel on EPIS is analyzed. Modeling of the gas channel transport leads to a spatial resolution of the model in x direction. The gas is transported through the gas

channel via convection and diffusion. As previously observed, the gas humidifier has a strong influence on the pressure response along the channel. To solely study the influence of the gas channel first, the humidifier is kept switched off.

Figures 3g and 3h compare simulated EPIS spectra of the time-independent model and the model considering the channel. In the frequency range below 1 Hz, the magnitude and phase shift are almost the same for both models. Above 1 Hz, the influence of the gas channel becomes visible and shows features in two different frequency ranges. The first feature can be observed in the frequency range between 1–10 Hz. The magnitude decreases which is accompanied by a local minimum in the phase shift of −10°. For further increasing frequency, the magnitude of the gas channel model shows a constant value between 10–100 Hz. Between 100–2000 Hz, the EPIS spectra show a rather complex behavior. The magnitude shows a decrease down to zero with a superimposed oscillation. In the same range, the phase shift shows a decrease down towards −180°, also accompanied by a superimposed oscillation.

The reason for the first feature at 1–10 Hz is not known at present. The origin of the second feature above 100 Hz can be explained by the following hypothesis. Above 100 Hz, the total pressure oscillates with a similar amplitude but different phase for different positions within the channel due to the finite velocity of pressure propagation. The phase shift of the pressure oscillation along the channel causes their effect on the cell voltage to cancel out. It should be stressed here that this feature is above the frequency range studied experimentally and also above the maximum frequency of the simulations in Fig. 1. The oscillation of the magnitude and phase shift with increasing frequency was also observed by Sun et al.,[26] in the context of the concentration admittance analysis and by Sorrentino,[27] in the context of concentration frequency response analysis.

When comparing the results of the gas channel model with that of the full model (Figs. 3g and 3h), it becomes clear that none of the features shown by the reduced model is present in the full model. The response of the full model is therefore not due to gas transport in the channel.

Humidifier and gas transport in the channel.—The final model configuration studied here is a combination of the gas channel (as in the previous subsection) and the humidifier upstream the cathode gas channel. Figures 3i and 3j compare simulated EPI spectra of the time-independent model to the model considering channel and humidifier. At the quasi-static frequency of 1 mHz, both model configurations show the same magnitude and phase shift. With increasing frequency, however, the influence of the humidifier becomes clearly visible by showing a strong increase of the magnitude from 0.3 μV Pa^{-1} to a maximum of 5.4 μV Pa^{-1} at 1 Hz. In the frequency range between 1–100 Hz the magnitude decreases back down to a value slightly below the magnitude of the quasi-static frequency. The phase shift shows a constant decrease from 0° at 1 mHz down to nearly −400° at 100 Hz.

A comparison of the spectra with and without the humidifier (Figs. 3g and 3i) shows the dominating influence of the humidifier on the EPIS results. Furthermore, a comparison of the spectra of the present model configuration with the spectra of the full model (Figs. 3i and 3j) reveals their strong similarity. Therefore, the most prominent EPIS features of the full model, the peak of magnitude (FOI 3) and the continuous decrease of phase shift with frequency (FOI 4), can be traced back to the humidifier. At frequencies above ca. 100 Hz, the EPIS magnitude of the reduced model shows a fine structure that is similar to that of the model with gas channel alone (Figs. 3g and 3i). This means that a channel signature can remain visible, but is largely masked by the humidifier.

To further interpret the features, the derivative of the cell voltage with respect to the pressure excitation (inserting Eqs. 4, 10 and 13 into 2) is again considered. For the given model configuration, the following simplifications can be made: no double layer capacity ($C_{\mathrm{DL}}^{\mathrm{V}} = 0$), constant conductivity of the electrolyte ($B = 0$, cf. Eq. 12), no gradients in y dimension. Using these assumptions, the derivative of the cell voltage with respect to the cathode outlet pressure is given by

$$\frac{\partial V_{\mathrm{cell}}}{\partial p_{\mathrm{CCH}}^{\mathrm{out}}} = \frac{RT}{F}\left(\frac{1}{4} + \frac{0.54}{\alpha_{\mathrm{C}}}\right)\frac{1}{p_{\mathrm{O_2,CL}}(x)}\frac{\partial p_{\mathrm{O_2,CL}}(x)}{\partial p_{\mathrm{CCH}}^{\mathrm{out}}} + \frac{RT}{\alpha_{\mathrm{C}}F}\frac{1}{-i_{\mathrm{elyt}}(x)}\frac{\partial i_{\mathrm{elyt}}(x)}{\partial p_{\mathrm{CCH}}^{\mathrm{out}}} + \frac{L_{\mathrm{PEM}}}{\sigma_{\mathrm{elyt}}}\frac{\partial i_{\mathrm{elyt}}(x)}{\partial p_{\mathrm{CCH}}^{\mathrm{out}}}. \quad [28]$$

The first term shows the influence of the oxygen pressure response while the second and third terms show the influence of ionic current density response. Again, if we assume that the change of ionic current density $\partial i_{\mathrm{elyt}}(x)/\partial p_{\mathrm{CCH}}^{\mathrm{out}}$ is only a local effect and is negligible for the overall fuel cell response, as discussed above in the context of Eq. 13, we can conclude that the cell voltage response here is dominated by the oxygen pressure response.

The coupled fuel cell/humidifier response.—The EPIS response $Z_{V/p}$ of the experimental fuel cell (cf. Fig. 1) shows a characteristic increase of magnitude (FOI 2) up to a maximum (FOI 3) and constant decrease of phase shift with frequency (FOI 4). In the previous section we have shown that this response is dominated by the humidifier and closely related to the oxygen pressure response. In this section we will demonstrate why the humidifier has such a dominating influence on EPIS, by demonstrating its effect on the oxygen pressure and thus cell voltage response. To this end, we will further analyze the coupled response of the fuel cell/humidifier system by means of internal states in the time domain and in the frequency domain.

Oscillations of internal states.—Figure 4 shows the simulated dynamics of a number of internal states during pressure excitation of the full model for three different frequencies of 1 mHz (quasi-static response), 1 Hz (resonance frequency of the main EPIS feature FOI 3, cf. Fig. 1) and 100 Hz (main feature fully relaxed, cf. Fig. 1). Humidifier and channel are shown schematically as orientation. The numbering of the panels (a), (b) etc. follows along causal links indicated by arrows, starting from the cathode channel outlet pressure excitation (panel a) and resulting in the voltage response (panel g). The causal links will be explained further below. We start the following discussion with the dynamics of $p_{\mathrm{CCH}}^{\mathrm{out}}$, shown in panel a). As the outlet pressure represents the boundary condition of the simulation, the time-normalized pressure curves of the different frequencies superimpose. The amplitude of pressure excitation is 100 Pa.

The pressure excitation at the outlet leads to a frequency-dependent response of pressure within the channel, shown at the channel inlet as $p_{\mathrm{CCH}}^{\mathrm{in}}$ in panel b), and as channel-averaged pressure $\bar{p}_{\mathrm{CCH}}$ in panel c). The model assumes negligible influence of the pipes between humidifier and fuel cell, therefore, $p_{\mathrm{CCH}}^{\mathrm{in}}$ is identical to the pressure in the humidifier. The simulated $p_{\mathrm{CCH}}^{\mathrm{in}}$ shows a significant frequency-dependent change of amplitude and phase shift compared to the exciting $p_{\mathrm{CCH}}^{\mathrm{out}}$. At high frequency, the channel inlet pressure oscillation is not visible anymore. Panel d) shows the mass flow rate $\dot{m}_{\mathrm{CCH}}^{\mathrm{in}}$ at the channel inlet. At low frequency, it shows a constant value corresponding to the stoichiometry-controlled mass

flow rate into the humidifier. At higher frequencies, it exhibits an oscillating behavior with varying amplitude and phase shift. The resulting channel-averaged oxygen molar fraction $\bar{x}_{O_2,CCH}$ is shown in panel e). It shows a distinct oscillation at 1 Hz, but neither at 1 mHz nor at 100 Hz. This state therefore clearly represents the resonance behavior. Panel f) shows the channel-averaged oxygen pressure $\bar{p}_{O_2,CCH}$, which is a result of the combined $\bar{p}_{CCH}$ (panel c) and $\bar{x}_{O_2,CCH}$ (panel e). Again, the resonance behavior is obvious. Finally, panel g) shows the resulting cell voltage V_{cell}. At 1 mHz, it oscillates with low amplitude in phase with the pressure excitation p_{CCH}^{out}. At the resonance frequency of 1 Hz, it oscillates with high amplitude and ca. 180° phase shift compared to p_{CCH}^{out}. At 100 Hz, V_{cell} oscillates only with a very low amplitude.

Taken the responses of the pressure excitation p_{CCH}^{out} and the cell voltage V_{cell} together leads to the overall EPIS signal $Z_{V/p}$ of the cell, as shown in Fig. 1. From the dynamic behavior of the internal states shown in Fig. 4, it can be seen that the main EPIS features, the increase of magnitude to its maximum (FOI 2) and the decrease in phase shift (FOI 4) can be traced back to a complex response of various internal states, predominantly the channel-averaged oxygen molar fraction $\bar{x}_{O_2,CCH}$ shown in Fig. 4e). In order to understand this behavior, we will further analyze the response in the following subsections using various transfer functions and additional simplified models.

Oxygen partial pressure response.—The relationship between the channel-averaged oxygen partial pressure $\bar{p}_{O_2,CCH}$ (Fig. 4f) and the pressure excitation p_{CCH}^{out} (Fig. 4a) can be further described using the transfer function $Z_{\bar{p}(O_2)/p}$, as defined in Eq. 14. This transfer function, calculated using simulation output from the full model, is shown in Bode representation in Fig. 5 (blue line; the other data sets shown in the figure will be discussed further below). It has qualitatively the same shape and features FOI 1–5 as the EPIS signal $Z_{V/p}$ (Fig. 1). This has already been pointed out in our previous paper.[18] The cell voltage is related to the partial pressure of oxygen through the equilibrium potential of the ORR (cf. Eq. 4) and through the ORR kinetics (cf. Eq. 10). The simplified relationship given in Eq. 24 even shows that $\partial V_{cell}/\partial p$ is directly proportional to $\partial p_{O_2}/\partial p$. The oscillation of the water partial pressure is of minor importance as it influences the cell voltage response only towards low frequencies due to the sluggish process of water uptake of the PEM (cf. Figs. 3c and 3d). This explains the self-similarity between $Z_{\bar{p}(O_2)/p}$ and $Z_{V/p}$.

In order to understand the response of the oxygen partial pressure, we continue by recognizing that it can be expressed as the product of the total pressure and the oxygen molar fraction according to

$$p_{O_2}(x) = p(x)x_{O_2}(x). \quad [29]$$

The derivative of the partial pressure with respect to the cathode outlet pressure follows as

$$\frac{\partial p_{O_2}(x)}{\partial p_{CCH}^{out}} = x_{O_2}(x)\frac{\partial p(x)}{\partial p_{CCH}^{out}} + p(x)\frac{\partial x_{O_2}(x)}{\partial p_{CCH}^{out}}. \quad [30]$$

From the right-hand side of this equation it can be seen that the change in oxygen partial pressure consists of two components, a change in total pressure, represented by the first term, and a change in molar fraction, represented by the second term. In the following, we want to consider the relationship of these two terms as a function of frequency. To this end, we use the following relationship in which we replaced the derivatives of Eq. 30 by the transfer functions defined in Eqs. 14–16:

$$Z_{\bar{p}(O_2)/p} = \bar{x}_{O_2}Z_{\bar{p}/p} + \bar{p}Z_{\bar{x}(O_2)/p}. \quad [31]$$

Instead of their locally resolved values, we used the average responses in the along-the-channel direction.

Figure 5 shows, in addition to $Z_{\bar{p}(O_2)/p}$, the simulated transfer functions of the two terms on the right-hand side of Eq. 31. At quasi-static response state (1 mHz), the transfer function $Z_{\bar{p}(O_2)/p}$ equals the transfer function $Z_{\bar{p}/p}$ multiplied by the average oxygen molar fraction, in both magnitude and phase. The magnitude of the transfer function $Z_{\bar{x}(O_2)/p}$ multiplied by the average total pressure approaches zero towards the lowest frequency. This means that the oxygen partial pressure oscillation is dominated by the total pressure oscillation $Z_{\bar{p}/p}$ (first term of Eq. 31), whereas the oxygen molar fraction is constant and does not oscillate. With increasing frequency, the molar fraction of oxygen starts to oscillate and contributes to the partial pressure oscillation of oxygen. Above 10 mHz, the partial pressure oscillation of oxygen gets increasingly dominated by the oscillation of the molar fraction $Z_{\bar{x}(O_2)/p}$ (second term of Eq. 31), which leads to the characteristic increase up to the maximum around 0.5 Hz.

The transition of the partial pressure oscillation $Z_{\bar{p}(O_2)/p}$ from being dominated by the total pressure oscillation $Z_{\bar{p}/p}$ to being dominated by the molar fraction oscillation $Z_{\bar{x}(O_2)/p}$ is also reflected in the phase shift. At 1 mHz, the phase shift of $Z_{\bar{p}(O_2)/p}$ is 0° and corresponds to the phase shift of $Z_{\bar{p}/p}$. With increasing frequency, the phase shift of $Z_{\bar{p}(O_2)/p}$ decreases and approaches the phase shift of $Z_{\bar{x}(O_2)/p}$. Around 0.5 Hz, the oscillation of the molar fraction and the total pressure are almost in antiphase (as indicated in the lower panel of Fig. 5). The antiphase is the reason why the maximum magnitude of the partial pressure oscillation is slightly below the maximum of the molar fraction oscillation multiplied by the average total pressure.

Above 0.5 Hz, the magnitude of $Z_{\bar{p}(O_2)/p}$ decreases due to the decrease of the magnitude of $Z_{\bar{x}(O_2)/p}$. As the amplitude of $Z_{\bar{x}(O_2)/p}$ tends to zero at 100 Hz, the influence of $Z_{\bar{p}/p}$ on $Z_{\bar{p}(O_2)/p}$ becomes visible again.

An interesting observation is the qualitative similarity of the transfer function $Z_{\bar{p}/p}$ and the EPIS spectra of Shirsath et al.[14–16] which they obtained for the operation of the fuel cell with pure oxygen instead of air. The magnitude shows a qualitatively similar progression between 1 mHz–1 Hz and the phase shift a quantitatively similar progression. This indicates that the oscillation of the molar fraction is insignificant for the operation with pure oxygen.

Oxygen molar fraction and inlet flow rate.—The analysis above shows that the oxygen partial pressure oscillation is dominated by the oxygen molar fraction oscillation. In this section, an interpretation of the oxygen molar fraction oscillation, including its amplitude and phase shift, is given. As the overall consumption and production of species per time under galvanostatic control is constant, the change in average molar fraction has to arise from a change in the supply. Shirsath et al.[16] observed that the air flow rate at the cathode inlet is varying during pressure excitation, even though the humidifier upstream the fuel cell is fed with a constant air flow rate. This is due to the gas volume in the humidifier, which acts as a gas reservoir with changing content for a change in pressure. In the following, first, the frequency dependence of the oscillating inlet flow rate is analyzed. Second, a simplified model is derived which allows the calculation of the molar fraction as a function of the inlet flow rate.

The oscillating inlet flow rate is analyzed by means of the transfer function $Z_{Q/p}$ between the inlet standard flow rate Q_{CCH}^{in}, as obtained from the full model, and the pressure excitation (cf. Eq. 17). Figure 6 shows $Z_{Q/p}$ as function of frequency (solid blue

line). The amplitude of the inlet flow rate oscillation approaches zero towards 1 mHz. Therefore, at the quasi-static frequency, the gas flow rate at the fuel cell inlet is constant, as given by the defined oxygen stoichiometry. With increasing frequency, the inlet flow rate starts to oscillate with an increasing amplitude. This finding can be explained using the mass conservation equation of the gas reservoir of the humidifier,

$$\frac{V_{\text{hum}}}{n_{\text{CH}}}\frac{\partial \rho_{\text{hum}}}{\partial t} = \dot{m}_{\text{feed}} - \dot{m}^{\text{in}}_{\text{CCH}}. \quad [32]$$

This equation shows that the temporal change of humidifier gas density ($\partial\rho_{\text{hum}}/\partial t$) equals the difference between the constant gas feed to the humidifier ($\dot{m}_{\text{feed}}$), and the flow rate out of the humidifier ($\dot{m}^{\text{in}}_{\text{CCH}}$, which is equal to the gas channel inlet flow rate). Following from the ideal gas law, the gas density ρ_{hum} is proportional to the gas pressure p_{hum}, which is equal to $p^{\text{in}}_{\text{CCH}}$ as per model assumption. Hence,

$$\dot{m}^{\text{in}}_{\text{CCH}} = \dot{m}_{\text{feed}} - a\frac{\partial p^{\text{in}}_{\text{CCH}}}{\partial t}, \quad [33]$$

where, a is a constant. This equation shows that $\dot{m}^{\text{in}}_{\text{CCH}}$ is directly related to the time-derivative of inlet pressure. Towards 1 mHz the change of pressure per time is so low that the inlet flow rate is constant, $\dot{m}^{\text{in}}_{\text{CCH}} = \dot{m}_{\text{feed}}$ (cf. Fig. 4d). With increasing frequency, the change of the pressure per time increases (although the amplitude of the inlet pressure oscillation decreases[16–18]), and the change of the inlet flow rate becomes significant, visible as the increase of magnitude of $Z_{Q/p}$.

The phase shift of $Z_{Q/p}$ is close to –90° at the lowest frequency and decreases with frequency down to a plateau of about –180° above 1 Hz. This progression of phase shift can be explained as follows. The change of the inlet flow rate is proportional to the time derivative of the inlet pressure (Eq. 33). Assuming that $p^{\text{in}}_{\text{CCH}}$ takes the form of a sine function, $\dot{m}^{\text{in}}_{\text{CCH}}$ will take the form of a cosine function, therefore a phase shift of –90°. Based on this explanation, the oscillating inlet flow rate follows the oscillation of the inlet pressure with an offset of –90° (cf. $Z_{p/p}$ in Refs. 16–18).

Figure 6 also shows a comparison between our simulations and an approximation of Shirsath et al.[16] derived on the base of an equivalent circuit model. They calculated the oscillating inlet flow rate according to

$$\Delta Q^{\text{in}}_{\text{CCH}}(t) = -C\omega|Z_{p/p}|\,\hat{p}^{\text{out}}_{\text{CCH}}\cos(\omega t + \phi(Z_{p/p})), \quad [34]$$

where Q is the flow rate and C a capacitive parameter proportional to the humidifier gas volume. It should be stressed here that Q describes the volumetric flow rate at standard conditions and thus has the unit of normal liter per seconds. The magnitude and phase shift of the transfer function $Z_{p/p}$ are

$$|Z_{p/p}| = \frac{1}{\sqrt{1 + (rC\omega)^2}} \quad [35]$$

and

$$\phi(Z_{p/p}) = -\text{atan}(rC\omega), \quad [36]$$

where $r = \Delta p/\Delta Q$ is a constant equivalent circuit model parameter representing the pressure drop along the channel per flow rate. For parametrization of the parameters r and C the reader is referred to Shirsath et al.[16] The results of the approximation of Shirsath et al. show a good agreement with our simulation, although there is a deviation in the magnitude above 0.1 Hz and in the phase shift above 10 Hz visible. Above 1 Hz, the amplitude of inlet flow rate oscillations is constant in case of the approximation of Shirsath et al., while the simulations show a further increase. The reason for this difference is unclear.

Qualitatively, the increase of magnitude of $Z_{Q/p}$ is similar to the increase of magnitude of $Z_{\bar{x}(\text{O}_2)/p}$ (cf. Fig. 5 red line). In order to quantify the relationship between these two transfer functions, we subsequently derive a simple model which allows the calculation of the molar fraction as a function of the inlet flow rate. The molar fraction of species i at position x can be expressed as the local ratio of the molar flow rate of species i and the total molar flow rate according to

$$x_{i,\text{CCH}}(x,t) = \frac{\dot{n}_{i,\text{CCH}}(x,t)}{\dot{n}_{\text{CCH}}(x,t)}. \quad [37]$$

To express both quantities as a function of the inlet flow rate, we use the molar balance of the gas phase from the inlet to position x. For the sake of simplicity, the following assumptions are made: The molar balance considers only the consumption and production of species along the channel due to the ORR, in which water is assumed to be produced directly in the gas phase. The sorption of water is neglected. The reaction rate of the ORR along the channel is assumed to be constant. Furthermore, the duration which is needed for the gas to pass the channel is assumed to be negligible, compared to the time period of one excitation wave. Thus, the change of the inlet flow rate is assumed to have an instant effect on the flow rate throughout the channel. Additionally, the inlet gas composition is assumed to be constant.

With these simplifications, the total molar flow rate at position x can be calculated as

$$\dot{n}_{\text{CCH}}(x,t) = \dot{n}^{\text{in}}_{\text{CCH}}(t) - \dot{n}^{\text{ORR}}_{\text{O}_2,\text{CCH}}(x) + \dot{n}^{\text{ORR}}_{\text{H}_2\text{O},\text{CCH}}(x), \quad [38]$$

where, $\dot{n}^{\text{ORR}}_{\text{O}_2,\text{CCH}}(x)$ is the molar rate of consumed oxygen and $\dot{n}^{\text{ORR}}_{\text{H}_2\text{O},\text{CCH}}(x)$ the molar rate of produced water due to the ORR from the channel inlet until position x. With the oxygen molar balance, the molar flow rate of oxygen at position x is calculated as

$$\dot{n}_{\text{O}_2,\text{CCH}}(x,t) = \dot{n}^{\text{in}}_{\text{CCH}}(t)x^{\text{in}}_{\text{O}_2,\text{CCH}} - \dot{n}^{\text{ORR}}_{\text{O}_2,\text{CCH}}(x). \quad [39]$$

In analogy, the molar flow rate of water at position x is calculated as

$$\dot{n}_{\text{H}_2\text{O},\text{CCH}}(x,t) = \dot{n}^{\text{in}}_{\text{CCH}}(t)x^{\text{in}}_{\text{H}_2\text{O},\text{CCH}} + \dot{n}^{\text{ORR}}_{\text{H}_2\text{O},\text{CCH}}(x). \quad [40]$$

The inlet flow rate is calculated as the sum of the constant molar flow rate into the humidifier $\dot{n}_{\text{feed}}$ and the oscillating inlet flow rate out of the humidifier:

$$\dot{n}^{\text{in}}(t) = \dot{n}_{\text{feed}} + \Delta Q^{\text{in}}_{\text{CCH}}(t)\frac{p_{\text{N}}}{RT_{\text{N}}}. \quad [41]$$

The oscillating inlet flow rate is calculated by the use of Eq. 34 and needs to be converted from normal volume flow into molar flow, with the standard pressure $p_{\text{N}} = 101\,325$ Pa and standard temperature $T_{\text{N}} = 273.15$ K. The constant molar flow rate into the humidifier under stoichiometric control can be calculated as

$$\dot{n}_{\text{feed}} = \frac{\lambda_{\text{O}_2}}{x^{\text{in}}_{\text{O}_2,\text{CCH}}}\frac{i_{\text{cell}}A_{\text{FC}}}{4F}, \quad [42]$$

where, λ_{O_2} is the oxygen stoichiometry. The consumption of oxygen due to the ORR from the inlet until position x is

$$\dot{n}^{\text{ORR}}_{\text{O}_2,\text{CCH}}(x) = \frac{1}{4F}i_{\text{cell}}A_{\text{FC}}\frac{x}{L_{\text{CH}}}. \quad [43]$$

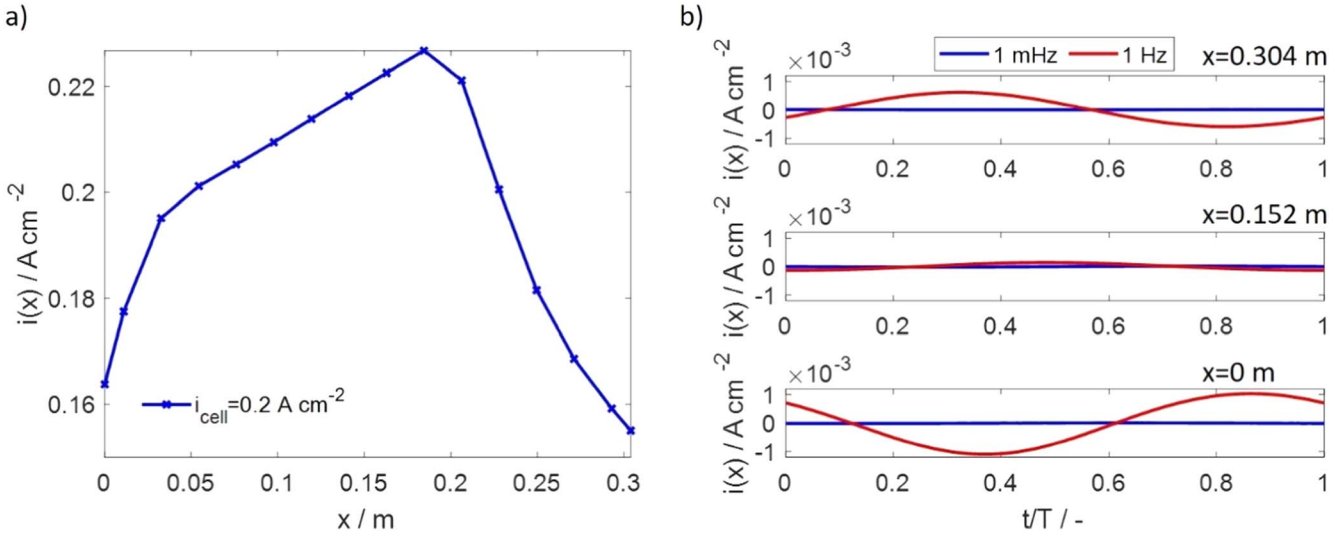

Figure 8. Simulated local current density at a total current density of 0.2 A cm^{-2}. (a) Local current density as function of channel dimension for constant outlet pressure (note that we increased the discretization for this simulation). (b) Local current density oscillation as function of time (normalized to period) during pressure excitation at three different channel locations (cathode inlet corresponds to 0.304 m).

In analogy, the production of water from the inlet until position x is

$$\dot{n}^{\mathrm{ORR}}_{\mathrm{H_2O,CCH}}(x) = \frac{1}{2F} i_{\mathrm{cell}} A_{\mathrm{FC}} \frac{x}{L_{\mathrm{CH}}}. \qquad [44]$$

For oxygen as the species of interest, the molar fraction at position x is given by combining Eqs. 37–44 to

$$x_{\mathrm{O_2}}(x,\, t) = \frac{x^{\mathrm{in}}_{\mathrm{O_2,CCH}} \Delta Q^{\mathrm{in}}_{\mathrm{CCH}}(t) \frac{p_{\mathrm{N}}}{RT_{\mathrm{N}}} + \frac{i_{\mathrm{cell}} A_{\mathrm{FC}}}{4F}\left(\lambda_{\mathrm{O_2}} - \frac{x}{L_{\mathrm{CH}}}\right)}{\Delta Q^{\mathrm{in}}_{\mathrm{CCH}}(t) \frac{p_{\mathrm{N}}}{RT_{\mathrm{N}}} + \frac{i_{\mathrm{cell}} A_{\mathrm{FC}}}{4F}\left(\frac{\lambda_{\mathrm{O_2}}}{x^{\mathrm{in}}_{\mathrm{O_2,CCH}}} + \frac{x}{L_{\mathrm{CH}}}\right)}. \qquad [45]$$

where, $\Delta Q^{\mathrm{in}}_{\mathrm{CCH}}(t)$ is taken from Eq. 34. With this expression, it is now possible to approximate the effect of the oscillating inlet flow rate on the molar fraction of oxygen along the channel.

Figure 7 shows the spectra of the resulting transfer function $Z_{\bar{x}(\mathrm{O_2})/p}$ at a current density of 0.2 A cm^{-2} as dashed red line, calculated by inserting Eqs. 45 into 16. The magnitude shows an increase from zero at the lowest frequency up to 1 Hz. Above 1 Hz, the magnitude remains constant. Figure 7 also shows $Z_{\bar{x}(\mathrm{O_2})/p}$ obtained from the full model (solid blue line). The two curves are very similar below 1 Hz. This shows that the increase of oxygen molar fraction oscillation with frequency can be traced back to the inlet flow rate oscillation. Above 1 Hz, the simulation shows a decrease of the magnitude towards zero at 100 Hz, which cannot be seen in the approximation through Eq. 45. One possible reason may be that towards higher frequencies, the duration of the gas transport through the gas channel is having an effect on the local molar fraction, which is neglected in the described approach of the simple model.

Taking a look at the phase shift of the approximated $Z_{\bar{x}(\mathrm{O_2})/p}$ reveals a decrease from −90° at 1 mHz to −180° around 1 Hz. Above 1 Hz, the phase shift remains −180°. The comparison with the full model simulation shift reveals again a good agreement below 1 Hz but diverges for frequencies above. Also, below 10 mHz, the simulation shows a different feature. This may be related to the assumption of constant inlet gas composition for the simplified model, which is not the case in the simulation.

To conclude, the increase of molar fraction oscillation along the gas channel observed in the simulations is caused by the increasingly oscillating inlet flow rate. This again affects the oxygen partial pressure response and hence the cell voltage response. Therefore, the characteristic increase of magnitude and decrease of phase shift of $Z_{V/p}$ in EPIS can finally be traced back to the oscillating inlet flow rate.

Local current oscillations.—A final note can be made on the spatiotemporal dynamics of the local current density. Kulikovsky recently claimed[28] that EPIS spectra may not be unique because "fixing a total current leads to a poorly defined problem which allows for multiple solutions depending on random fluctuations of local current."[28] We would like to emphasize that with our present model, we did not observe random fluctuations or ill-defined solutions. In fact, our model *predicts* the spatially-dependent (in channel dimension) current density distribution as simulation *output*. Simulated local current density as function of channel length at 0.2 A cm^{-2} and constant pressure is shown in Fig. 8a. It exhibits a nonlinear behavior, having a maximum around channel center. Figure 8b shows the oscillations around the static values when cathode outlet pressure is excited. The oscillation amplitude is around a factor of 100 smaller than the absolute value shown in panel a) and shows different phases for different positions along the channel.

In his simulations, Kulikovsky[28] *assumed* a stochastic current density distribution as model *input*. In contrast, in our present model, local current density is fully determined by the closed mathematical equation system (cf. Appendix); in particular, it depends, via the Butler-Volmer equation, on local activation overpotential and local concentrations, while the spatially averaged current density is equal to the cell current density applied as boundary condition. This results in a spatiotemporally nonlinear, but well-defined behavior, as shown in Fig. 8.

Conclusions

EPIS is an emerging tool for the diagnosis of polymer electrolyte membrane fuel cells (PEMFC). The present study aimed at a deeper understanding of the origin of observed features in the EPI spectra, which is a requirement for a qualitative and quantitative interpretation of EPIS. Using combined investigations of numerical simulations with a P2D model at different model reduction steps, analytical derivation of pressure-voltage relationships, visualization of internal states as function of time, and calculation of various transfer functions, we were able to draw the following conclusions.

• The quasi-static EPIS magnitude ($\lim_{f \to 0} |Z_{V/p}|$) (FOI 1 in Fig. 1) depends nonlinearly on current density. It is composed of three main contributions, originating from the cathode equilibrium potential, the cathode overpotential, and the electrolyte potential drop. The cathode equilibrium potential dominates at OCV, the cathode overpotential at intermediate current densities, and the electrolyte potential drop at high current densities. The contributions can be quantified using appropriate analytical expressions.

• The main EPIS feature, a dominant peak of $|Z_{V/p}|$ at around 1 Hz (FOI 2 and 3 in Fig. 1), is caused by the air humidifier upstream the cathode. We were able to interpret this behavior as a complex interdependence between various dynamic cell states: The cathode backpressure excitation causes a pressure oscillation in the humidifier, which causes an oscillation of the channel inflow rate that increases with frequency (FOI 2). The oscillating inflow rate triggers a resonance of the oxygen molar fraction, which transfers to a resonating oxygen partial pressure, which causes a resonating cell voltage (FOI 3).

• The EPIS signal shows a continuous decrease of the phase shift $\phi(Z_{V/p})$ from 0° at quasi-static frequency down to ca. −180° at the resonance frequency, and further down to ca. −400° at 100 Hz (FOI 4 in Fig. 1). This behavior is caused by a combination of the humidifier (up to ca. 10 Hz) and the electrical double layer (above ca. 10 Hz). The phase angle shows a certain fine structure above ca. 1 Hz, caused by the gas channel.

• The EPIS magnitude $|Z_{V/p}|$ shows a drop to zero towards high frequencies (FOI 5 in Fig. 1). Again, this is mainly caused by the humidifier. Above ca. 10 Hz, the response of the electrical DL contributes to the final drop.

• Water uptake into the PEM causes an EPIS feature at around 50 mHz. The gas channel causes two EPIS features at around 5 Hz and between 100–1000 Hz. The gas diffusion layer causes an EPIS feature at about 1 kHz. All these features are masked by the humidifier (10 mHz to 10 Hz) and by the DL (above 10 Hz).

• The DL shows the same characteristic frequency in EPIS as in "classical" EIS.

The present analysis was carried out on, and these conclusions are therefore valid for, a specific PEMFC single cell (100 cm^2 PEMFC, Nafion membrane, serpentine flow field) at common operating conditions (55 °C, dry hydrogen, humidified air, 0.2 A cm^{-2}, 850 ml humidifier gas volume). EPIS has been shown experimentally to strongly depend on cell geometries, materials, and operating conditions.[13–16,18,19] It should also be noted that the present model showed discrepancies with experimental data at higher current density (above ca. 0.5 A cm^{-2}).[18] The present study is therefore an important, yet still limited step towards fully understanding EPIS of PEMFC, and leaves ample room for further investigations.

Acknowledgments

The authors acknowledge funding from the German Research Foundation (Deutsche Forschungsgemeinschaft, DFG) (grant BE 3819/6–1) in the framework of the EPISTEL project.

Appendix. PEMFC Model

This study uses a parameterized and validated model of a PEMFC published before.[18] In order for the present paper to be self-consistent, this Appendix provides a complete summary of the model. Figure A·1 shows the P2D modeling domain. Table A·I gives all model equations. Table A·II gives the boundary conditions for the transport equations. Table A·III shows all parameters. Finally, a list of symbols is given in Table A·IV. A detailed model description, including derivation of model equations, determination of parameters, and all original references is given in Ref. 18.

Table A·I. Governing model equations. HOR, hydrogen oxidation reaction; ORR, oxygen reduction reaction.

Electrochemistry	
Reaction equation ORR	$\frac{1}{2}O_2(g) + 2H^+(elyt) + 2e^-(elde) \rightleftharpoons H_2O(elyt)$
Reaction equation HOR	$H_2(g) \rightleftharpoons 2H^+(elyt) + 2e^-(elde)$
Volumetric Faradaic current density (BV)	$i_F^V = i_0^V \left(\exp\left[\frac{\alpha_A F}{RT} \eta \right] - \exp\left[-\frac{\alpha_C F}{RT} \eta \right] \right)$
Volumetric DL charge/discharge current density	$i_{DL}^V = C_{DL}^V \frac{\partial(\Delta\phi)}{\partial t}$
Overpotential	$\eta = \Delta\phi - \Delta\phi^{eq}$
Galvani potential	$\Delta\phi = \phi_{elde} - \phi_{elyt}$
Equilibrium potential ORR	$\Delta\phi_{ORR}^{eq} = -\frac{\Delta H_{ORR} - T\Delta S_{ORR}}{2F} + \frac{RT}{2F} \ln\left(\sqrt{\frac{p_{O_2}}{p_{ref}}} \right)$
Equilibrium potential HOR	$\Delta\phi_{HOR}^{eq} = \frac{\Delta H_{HOR} - T\Delta S_{HOR}}{2F} - \frac{RT}{2F} \ln\left(\frac{p_{H_2}}{p_{ref}} \right)$
Charge transport (*y*direction)	
Potential gradient electrolyte	$\nabla\phi_{elyt} = -\frac{i_{elyt}}{\sigma_{elyt}}$
Potential gradient electrode	$\nabla\phi_{elde} = 0$
Charge conservation	$\nabla i_{elyt} = i_F^V + i_{dl}^V$
Cell voltage	$V_{cell} = \phi_{elde,C} - \phi_{elde,A} - i_{cell} R_{contact}$
Cell current density	$i_{cell} = -\frac{1}{L_{CH}} \int_{x=0}^{L_{CH}} \int_{y=0}^{L_{CL}} (i_F^V + i_{DL}^V) \mathrm{d}y\mathrm{d}x$
Gas transport in gas channels (*x*direction)	
Mass conservation	$\frac{\partial \rho}{\partial t} = -\nabla(\rho v) + \sum_{i=1}^{N} \dot{s}_i$
Species conservation	$\frac{\partial \rho_i}{\partial t} = -\nabla(\rho_i v) - \nabla j_i^{diff} + \dot{s}_i$
Momentum conservation	$\frac{\partial(\rho v)}{\partial t} = -\nabla(\rho v^2) - \nabla p - \frac{P_{ch}}{A_{ch}} \tau_w$
Gas exchange between gas channel and GDL	$\dot{s}_i = -\frac{w_{CH} + w_{rib}}{A_{CH}} J_i^{CH\|GDL} M_i$
Diffusive flux (Maxwell-Stefan)	

Table A·I. (Continued).

Electrochemistry	
	$\nabla x_i = -\sum_{j=1}^{N} \frac{1}{cD_{ij}}\left(\frac{x_j j_i^{\text{diff}}}{M_i} - \frac{x_i j_j^{\text{diff}}}{M_j}\right),\ \sum j_i^{\text{diff}} = 0$
Gas-phase transport in the porous layers (*y* direction)	
Species conservation	$\frac{\partial(\epsilon c_i)}{\partial t} = -\nabla(J^{\text{conv}} x_i) - \nabla J_i^{\text{diff}} + \dot{S}_i$
Convective flux (Darcy's law)	$J^{\text{conv}} = -c\frac{\kappa}{\mu}\nabla p$
Diffusive flux (Maxwell-Stefan)	$\nabla x_i = -\sum_{j=1}^{N} \frac{1}{cD_{ij}^{\text{eff}}}(x_j J_i^{\text{diff}} - x_i J_j^{\text{diff}}),\ \sum J_i^{\text{diff}} = 0$
Effective diffusion coefficients	$D_{ij}^{\text{eff}} = D_{ji}^{\text{eff}} = \frac{\varepsilon}{\tau^2}\frac{1}{2}\left(\frac{1}{1/D_i^K + 1/D_{ij}} + \frac{1}{1/D_j^K + 1/D_{ji}}\right)$
Source term gaseous hydrogen (ACL)	$\dot{S}_{\text{H}_2} = -\frac{i_{\text{F}}^{\text{V}}}{2F}$
Source term gaseous oxygen (CCL)	$\dot{S}_{\text{O}_2} = \frac{i_{\text{F}}^{\text{V}}}{4F}$
Source term gaseous water (ACL & CCL)	$\dot{S}_{\text{H}_2\text{O}} = -\frac{k_{\text{a,d}}}{L_{\text{CL}} V_{\text{m}}}(\lambda_{\text{eq}} - \lambda)$
Water transport in the electrolyte (*y* direction)	
Dissolved water conservation	$\frac{\partial \lambda}{\partial t}\frac{\epsilon_{\text{elyt}}}{V_{\text{m}}} = -\nabla J_\lambda^{\text{diff}} - \nabla J_\lambda^{\text{drag}} + \dot{S}_\lambda$
Diffusive flux	$J_\lambda^{\text{diff}} = -\frac{D_\lambda}{V_{\text{m}}}\nabla\lambda$
Electro-osmotic drag	$J_\lambda^{\text{drag}} = \frac{\xi}{F} i_{\text{elyt}}$
Source term dissolved water (ACL)	$\dot{S}_\lambda = \left\{\frac{k_{\text{a,d}}}{L_{\text{CL}} V_{\text{m}}}(\lambda^{\text{eq}} - \lambda)\right.$
Source term dissolved water (CCL)	$\dot{S}_\lambda = \frac{k_{\text{a,d}}}{L_{\text{CL}} V_{\text{m}}}(\lambda^{\text{eq}} - \lambda) - \frac{i_{\text{F}}^{\text{V}}}{2F}$
Humidifier	
Mass conservation	$v_{\text{CH}}^{\text{in}} = \frac{\left(\dot{m}_{\text{feed}} - \frac{V_{\text{hum}}}{n_{\text{CH}}}\frac{\partial \rho_{\text{CH}}^{\text{in}}}{\partial t}\right)}{A_{\text{ch}}\rho_{\text{CH}}^{\text{in}}}$
Mass feed rate	$\dot{m}_{\text{feed}} = \frac{\lambda_i}{x_{i,\text{CH}}^{\text{in}}}\frac{i A_{\text{FC}}}{z_i F n_{\text{CH}}}\bar{M}_{\text{CH}}^{\text{in}}$

Table A·II. Boundary conditions for the conservation equations.

Electrolyte charge transport (*y* direction)	$i_{\text{elyt}}^{\text{CGDL}\|\text{CCL}} = i_{\text{elyt}}^{\text{ACL}\|\text{AGDL}} = 0$
Gas transport channel (*x* direction)	$v_{\text{CCH}}^{\text{in}},\ v_{\text{ACH}}^{\text{in}}$
	$p_{\text{CCH}}^{\text{out}},\ p_{\text{ACH}}^{\text{out}}$
	$x_{\text{O}_2,\text{CCH}}^{\text{in}} = x_{\text{O}_2,\text{CCH}}^{\text{in,dry}}(1 - x_{\text{H}_2\text{O},\text{CCH}}^{\text{in}})$
	$x_{\text{N}_2,\text{CCH}}^{\text{in}} = x_{\text{N}_2,\text{CCH}}^{\text{in,dry}}(1 - x_{\text{H}_2\text{O},\text{CCH}}^{\text{in}})$
	$x_{\text{H}_2\text{O},\text{CCH}}^{\text{in}} = \varphi_{\text{CCH}}^{\text{in}}\frac{p_{\text{H}_2\text{O}}^{\text{sat}}}{p_{\text{CCH}}^{\text{in}}}$
	$x_{\text{H}_2,\text{ACH}}^{\text{in}} = x_{\text{H}_2,\text{ACH}}^{\text{in,dry}}(1 - x_{\text{H}_2\text{O},\text{ACH}}^{\text{in}})$
	$x_{\text{H}_2\text{O},\text{ACH}}^{\text{in}} = \varphi_{\text{ACH}}^{\text{in}}\frac{p_{\text{H}_2\text{O}}^{\text{sat}}}{p_{\text{ACH}}^{\text{in}}}$
Gas transport electrode (*y* direction)	$J_i^{\text{diff,CCL}\|\text{PEM}} = J_i^{\text{diff,PEM}\|\text{ACL}} = 0$
	$J^{\text{conv,CCL}\|\text{PEM}} = J^{\text{conv,PEM}\|\text{ACL}} = 0$
	$c_i^{\text{CCH}\|\text{CGDL}} = c_{\text{CCH},i},\ c_i^{\text{ACH}\|\text{AGDL}} = c_{\text{ACH},i}$
	$p^{\text{CGDL}\|\text{CCH}} = p_{\text{CCH}},\ p^{\text{AGDL}\|\text{ACH}} = p_{\text{ACH}}$
Dissolved water transport electrolyte (*y* direction)	$J_\lambda^{\text{CGDL}\|\text{CCL}} = J_\lambda^{\text{ACL}\|\text{AGDL}} = 0$

Table A·III. Model parameters.

Electrochemistry	
Exchange current density ORR	$i_{0,\mathrm{ORR}}^{\mathrm{V}} = 1.55{\cdot}10^{6}\frac{\mathrm{A}}{\mathrm{m}^3}\left(\frac{p_{\mathrm{O_2}}}{p_{\mathrm{ref}}}\right)^{0.54}\exp\left(\frac{67\frac{\mathrm{kJ}}{\mathrm{mol}}}{R}\left(\frac{1}{T_{\mathrm{ref}}}-\frac{1}{T}\right)\right)$
Exchange current density HOR	$i_{0,\mathrm{HOR}}^{\mathrm{V}} = 2.7{\cdot}10^{3}\frac{\mathrm{A}}{\mathrm{m}_{\mathrm{Pt}}^2}{\cdot}10^{7}\frac{\mathrm{m}_{\mathrm{Pt}}^2}{\mathrm{m}^3}\exp\left(\frac{16\frac{\mathrm{kJ}}{\mathrm{mol}}}{R}\left(\frac{1}{T_{\mathrm{ref}}}-\frac{1}{T}\right)\right)$
Anodic transfer coefficient	$\alpha_{\mathrm{A,ORR}} = 1.434,\ \alpha_{\mathrm{A,HOR}} = 1$
Cathodic transfer coefficient	$\alpha_{\mathrm{C,ORR}} = 0.566,\ \alpha_{\mathrm{C,HOR}} = 1$
Reaction enthalpy	$\Delta H_{\mathrm{ORR}} = -285.83\ \frac{\mathrm{kJ}}{\mathrm{mol}},\ \Delta H_{\mathrm{HOR}} = 0\ \frac{\mathrm{kJ}}{\mathrm{mol}}$
Reaction entropy	$\Delta S_{\mathrm{ORR}} = -163.3\ \frac{\mathrm{J}}{\mathrm{mol\ K}},\ \Delta S_{\mathrm{HOR}} = 0.104\frac{\mathrm{J}}{\mathrm{mol\ K}}$
Double layer capacity	$C_{\mathrm{DL}}^{\mathrm{V}} = 4.1{\cdot}10^{7}\ \mathrm{F/m^3}$
Charge transport	
Electrolyte conductivity	$\sigma_{\mathrm{elyt}} = \epsilon_{\mathrm{elyt}}^{1.5}(0.5139\lambda - 0.326)\exp\left(1268\left(\frac{1}{303}-\frac{1}{T}\right)\right)$, for $\lambda \geqslant 1$ $\sigma_{\mathrm{elyt}} = \sigma_{\mathrm{elyt}}(\lambda = 1)$, for $\lambda < 1$
Contact resistance	$R_{\mathrm{contact}} = 6.3{\cdot}10^{-6}\ \Omega\ \mathrm{m^2}$
Mass transport	
Wall shear stress gas channel	$\tau_{\mathrm{w}} = \frac{1}{8}\frac{P_{\mathrm{CH}}}{A_{\mathrm{CH}}}\mu v f_1 + \frac{1}{2}\rho v^2 f_2$
Friction factors	$f_1 = 18.5,\ f_2 = 0.021$
Permeability porous layers	$\kappa = \frac{\epsilon^3 d_{\mathrm{particle}}^2}{72\tau(1-\epsilon)^2}$
Knudsen diffusion coefficient	$D_i^K = \frac{2}{3}r_{\mathrm{pore}}\left(\frac{8}{\pi}\frac{RT}{M_i}\right)^{\frac{1}{2}}$
Diffusion coefficient water in electrolyte	$D_\lambda = \begin{cases} 3.1{\cdot}10^{-7}\frac{\mathrm{m^2}}{\mathrm{s}}{\cdot}\epsilon_{\mathrm{elyt}}^{1.5}\,\lambda(-1+\exp(0.28\lambda))\exp\left(-\frac{2436\ \mathrm{K}}{T}\right) & \text{for } \lambda \leqslant 3 \\ 4.17{\cdot}10^{-8}\ \frac{\mathrm{m^2}}{\mathrm{s}}{\cdot}\epsilon_{\mathrm{elyt}}^{1.5}\,\lambda(1+161{\cdot}\exp(-\lambda))\exp\left(-\frac{2436\ \mathrm{K}}{T}\right) & \text{for } \lambda > 3 \end{cases}$
Electro-osmotic drag coefficient	$\xi = \frac{2.5\lambda}{22}$
Water transfer coefficient (sorption)	$k_{\mathrm{a,d}} = a_{\mathrm{a,d}} f\exp\left[\frac{20\frac{\mathrm{kJ}}{\mathrm{mol}}}{R}\left(\frac{1}{T_{\mathrm{ref}}}-\frac{1}{T}\right)\right]$
kinetic parameter absorption/desorption	$a_{\mathrm{a}} = 3.53{\cdot}10^{-5}\frac{\mathrm{m}}{\mathrm{s}},\ a_{\mathrm{d}} = 1.42{\cdot}10^{-4}\frac{\mathrm{m}}{\mathrm{s}}$
Volume fraction of water	$f = \frac{\lambda V_{\mathrm{w}}}{\lambda V_{\mathrm{w}} + V_{\mathrm{m}}}$
Volume per sulfonic acid sides of the electrolyte	$V_{\mathrm{m}} = EW/\rho_{\mathrm{elyt,dry}}$
Equivalent weight	$EW = 1.02\ \mathrm{kg/equiv.}$
Density of dry electrolyte	$\rho_{\mathrm{elyt,dry}} = 1.97{\cdot}10^{3}\ \mathrm{kg\ m^{-3}}$
Molar volume of water	$V_{\mathrm{w}} = M_{\mathrm{H_2O}}/\rho_{\mathrm{H_2O}}$
Equilibrium water content electrolyte (ACL & CCL)	$\lambda^{\mathrm{eq}} = \begin{cases} 0.043 + 17.81a - 39.85a^2 + 36.0a^3, & \text{for } a \leqslant 1 \\ 14 + 1.4(a-1), & \text{for } 1 < a \leqslant 3 \end{cases}$
Water activity	$a = p_{\mathrm{H_2O}}/p_{\mathrm{H_2O}}^{\mathrm{sat}}(T)$
Geometries	
Fuel cell area	$A_{\mathrm{FC}} = (w_{\mathrm{CH}} + w_{\mathrm{rib}})L_{\mathrm{CH}}n_{\mathrm{CH}}$
Layer thickness	$L_{\mathrm{GDL}} = 212.5\ \mu\mathrm{m},\ L_{\mathrm{CL}} = 10\ \mu\mathrm{m},\ L_{\mathrm{PEM}} = 50\ \mu\mathrm{m}$
Porosity	$\varepsilon_{\mathrm{GDl}} = 0.77,\ \varepsilon_{\mathrm{Cl}} = 0.4$
Tortuosity	$\tau_{\mathrm{GDl}} = 1.26,\ \tau_{\mathrm{Cl}} = 1.26$
Volume fraction electrolyte	$\epsilon_{\mathrm{elyt,CL}} = 0.3,\ \epsilon_{\mathrm{elyt,PEM}} = 1.0$
Particle diameter	$d_{\mathrm{particle,GDL}} = 0.54\ \mu\mathrm{m},\ d_{\mathrm{particle,CL}} = 0.54\ \mu\mathrm{m}$
Pore radius	$r_{\mathrm{pore,GDL}} = 0.27\ \mu\mathrm{m},\ d_{\mathrm{pore,CL}} = 0.27\ \mu\mathrm{m}$
Channel length	$L_{\mathrm{CH}} = 0.304\ \mathrm{m}$
Channel cross-section area	$A_{\mathrm{CH}} = 3.08{\cdot}10^{-7}\ \mathrm{m^2}$
Channel width	$w_{\mathrm{CH}} = 0.7\ \mathrm{mm}$
Channel rib width	$w_{\mathrm{rib}} = 0.73\ \mathrm{mm}$
Channel wetted perimeter	$P_{\mathrm{CH}} = 2.28\ \mathrm{mm}$
Number of channels	$n_{\mathrm{CH}} = 23$
Gas phase volume humidifier	$V_{\mathrm{hum,A}} = 0\ \mathrm{ml}\ ,\ V_{\mathrm{hum,C}} = 850\ \mathrm{ml}$
Operating conditions	
Temperature	$T = 328.15\ \mathrm{K}$
Outlet pressure	$p_{\mathrm{CH}}^{\mathrm{out}} = 116\,325\ \mathrm{Pa}$

Table A·III. (Continued).

Electrochemistry	
Inlet relative humidity	$\varphi^{\text{in}}_{\text{ACH}} = 0.05,\ \varphi^{\text{in}}_{\text{CCH}} = 0.55$
Inlet mixture (dry) anode	$x_{\text{H}_2} = 1$
Inlet mixture (dry) cathode	$x_{\text{O}_2} = 0.21,\ x_{\text{N}_2} = 0.79$
Inlet stoichiometry	$\lambda_{\text{H}_2} = 1.2,\ \lambda_{\text{O}_2} = 2.5$
Constants	
Reference temperature	$T_{\text{ref}} = 353.15$ K
Reference pressure	$p_{\text{ref}} = 101\,325$ Pa
Ideal gas constant	$R = 8.314$ J/(mol K)
Faraday constant	$F = 96\,485$ C/mol

Table A·IV. List of symbols.

Latin	
A_{ch}	Cross-sectional area of gas channel, m^2
A_{FC}	Fuel cell area, m^2
a	Water activity, $-$
$a_{\text{a,d}}$	Water absorption/desorption rate coefficient, $\frac{\text{m}}{\text{s}}$
C^{V}_{DL}	Volume-specific double-layer capacitance, $\frac{\text{F}}{\text{m}^3}$
c, c_i	Gas concentration (of species i), $\frac{\text{mol}}{\text{m}^3}$
C	Capacitive parameter (EC model Shirsath et al.), 0.7241 Nl bar^{-1}
D_{ij}	Binary diffusion coefficient of species i and j, $\frac{\text{m}^2}{\text{s}}$
D^{eff}_{ij}	Effective binary diffusion coefficient of species i and j, $\frac{\text{m}^2}{\text{s}}$
D^{K}_{i}	Knudsen diffusion coefficient of species i, $\frac{\text{m}^2}{\text{s}}$
D_{λ}	Diffusion coefficient of water in ionomer, $\frac{\text{m}^2}{\text{s}}$
d_{particle}	Diameter of particle in porous electrode, m
EW	Equivalent weight of the dry ionomer, $\frac{\text{kg}}{\text{mol}}$
F	Faraday's constant, $96485\frac{\text{C}}{\text{mol}}$
f	Volume fraction of water in ionomer, $-$
f_1, f_2	Friction factors of gas channel, $-$
ΔH	Reaction enthalpy, $\frac{\text{J}}{\text{mol}}$
$i(x)$	Locall current density, $\frac{\text{A}}{\text{m}^2}$
i_{cell}	Cell current density, $\frac{\text{A}}{\text{m}^2}$
i_{elyt}	Ionic current density, $\frac{\text{A}}{\text{m}^2}$
i^{V}_{F}	Volume-specific Faradaic current density, $\frac{\text{A}}{\text{m}^3}$
i^{V}_{0}	Volume-specific exchange current density, $\frac{\text{A}}{\text{m}^3}$
i^{V}_{DL}	Volume-specific current density due to double layer charge/discharge, $\frac{\text{A}}{\text{m}^3}$
J^{conv}	Convective molar flux, $\frac{\text{mol}}{\text{m}^2\text{s}}$
J^{diff}_{i}	Diffusive molar flux of species i, $\frac{\text{mol}}{\text{m}^2\text{s}}$
$J^{\text{diff}}_{\lambda}$	Diffusive molar flux of water in the ionomer, $\frac{\text{mol}}{\text{m}^2\text{s}}$
$J^{\text{drag}}_{\lambda}$	Molar flux of water dragged in the ionomer, $\frac{\text{mol}}{\text{m}^2\text{s}}$
j^{diff}_{i}	Diffusive mass flux of species i, $\frac{\text{kg}}{\text{m}^2\text{s}}$
$k_{\text{a,d}}$	Water absorption/desorption rate constant, $\frac{\text{m}}{\text{s}}$
L	Length, thickness, m
M_i	Molar mass of species i, $\frac{\text{kg}}{\text{mol}}$
$\dot{m}$	Mass flow rate, $\frac{\text{kg}}{\text{s}}$
$\dot{m}_{\text{feed}}$	Mass flow rate into gas phase humidifier, $\frac{\text{kg}}{\text{s}}$
n_{CH}	Number of gas channels, $-$

Table A·IV. (Continued).

Latin	
$\dot{n}$, $\dot{n}_i$	(Partial) molar flow rate (of species) i, mol s^{-1}
$\dot{n}_{\text{feed}}$	Molar flow rate into gas phase humidifier, mol s^{-1}
P_{ch}	Channel perimeter, m
p, p_i	(Partial) pressure (of species i), Pa
$p_{H_2O}^{\text{sat}}$	Saturation pressure of water, Pa
p_{ref}	Reference pressure in Nernst equation, 101 325 Pa
$\hat{p}_{\text{CCH}}^{\text{out}}$	Pressure excitation amplitude (EC-model Shirsath et al.), Pa
Q	Standard flow rate, Nl s^{-1}
r	Pressure drop per flow rate (EC model Shirsath et al.), 1.417 bar s Nl^{-1}
R	Ideal gas constant, 8.314 $\frac{\text{J}}{\text{mol K}}$
R_{contact}	Specific contact resistance, $\Omega\,m^2$
r_{pore}	Pore radius of porous electrode, m
ΔS	Reaction entropy, $\frac{\text{J}}{\text{mol K}}$
$\dot{S}_i$	Molar source term of species i, $\frac{\text{mol}}{\text{m}^3\text{s}}$
$\dot{S}_\lambda$	Molar source term of water in the ionomer, $\frac{\text{mol}}{\text{m}^3\text{s}}$
$\dot{s}_i$	Mass source term of species i, $\frac{\text{kg}}{\text{m}^3\text{s}}$
T	Temperature, K
T_{ref}	Reference temperature in kinetic expressions, 353.15 K
t	Time, s
V_{cell}	Cell voltage, V
V_{hum}	Gas phase volume of humidifier, m^3
V_{m}	Volume per sulfonic acid sides of the ionomer, $\frac{\text{m}^3}{\text{mol}}$
V_{w}	Molar volume of water, $\frac{\text{m}^3}{\text{mol}}$
v	Channel flow velocity, $\frac{\text{m}}{\text{s}}$
w_{CH}	Channel width, m
w_{rib}	Channel rib width, m
x_i	Molar fraction of species i, –
$Z_{V/i}$	Transfer function: electrochemical impedance, $\Omega\,m^2$
$Z_{V/p}$	Transfer function: electrochemical pressure impedance, $\frac{\text{V}}{\text{Pa}}$
$Z_{p/p}$	Transfer function: inlet pressure - outlet pressure, –
$Z_{\bar{p}/p}$	Transfer function: average (CCH) pressure - outlet pressure, –
$Z_{\bar{p}(O_2)/p}$	Transfer function: average (CCH) oxygen pressure - outlet pressure, –
$Z_{Q/p}$	Transfer function: standard inlet flow rate - outlet pressure, –
$Z_{\bar{x}(O_2)/p}$	Transfer function: average (CCH) oxygen molar fraction - outlet pressure, –
Greek	
α	Transfer coefficient half-cell reaction, –
ε	Porosity of porous electrode, –
ϵ_{elyt}	Volume fraction of the ionomer, –
η	Overpotential, V
κ	Permeability of the porous electrode, m^2
λ	Water content of the ionomer, –
λ^{eq}	Water content of the ionomer at equilibrium, –
λ_i	Inlet stoichiometry of species i, –
μ	Viscosity of gas, $\frac{\text{kg}}{\text{m s}}$
ξ	Electro-osmotic drag coefficient, –
ρ, ρ_i	Gas density (of species i), $\frac{\text{kg}}{\text{m}^3}$
$\rho_{\text{elyt,dry}}$	Mass density of the dry ionomer, $\frac{\text{kg}}{\text{m}^3}$
σ_{elyt}	Proton conductivity of the ionomer, $\frac{\text{S}}{\text{m}}$
τ	Geometric tortuosity of porous electrode, –
τ_{w}	Wall shear stress, Pa
ϕ	Electric potential, V
$\phi(Z)$	Phase shift of transfer function Z, °
$\Delta\phi$	Galvani potential, V
$\Delta\phi^{\text{eq}}$	Galvani potential at equilibrium, V
$\Delta\phi_{\text{elyt}}$	Potential difference across the electrolyte, V

Table A·IV. (Continued).

Latin	
φ	Relative humidity, $^-$
ω	Angular frequency, s^{-1}
Subscripts/superscripts	
A	Anode
C	Cathode
CH	Gas channel
CL	Catalyst layer
elde	Electrode
elyt	Electrolyte
dry	Quantity is related to dry conditions
GDL	Gas diffusion layer
HOR	Hydrogen oxidation reaction
hum	Humidifier
in	Inlet of gas channel
ORR	Oxygen reduction reaction
out	Outlet of gas channel
PEM	Polymer electrolyte membrane layer

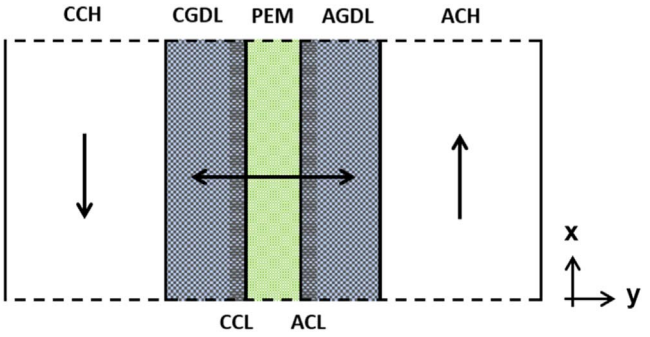

Figure A·1. Schematic representation of the 1D+1D modeling domain with indicated mass transport directions through layers cathode/anode gas channel (CCH/ACH), cathode/anode gas diffusion layer (CGDL/AGDL), cathode/anode catalyst layer (CCL/ACL), and polymer electrolyte membrane (PEM). The figure is extracted from Ref. 18.

ORCID

Lutz Schiffer https://orcid.org/0000-0002-0187-5031
Wolfgang G. Bessler https://orcid.org/0000-0001-8037-9046

References

1. S. Schiebahn, T. Grube, M. Robinius, V. Tietze, B. Kumar, and D. Stolten, *Int. J. Hydrogen. Energy*, **40**, 4285 (2015).
2. K. Knosala, L. Kotzur, F. T. C. Röben, P. Stenzel, L. Blum, M. Robinius, and D. Stolten, *Int. J. Hydrogen. Energy*, **46**, 21748 (2021).
3. E4tech, *The Fuel Cell Industry Review 2021* (2022), (https://fuelcellindustryreview.com/).
4. S. J. Andreasen, J. R. Vang, and S. K. Kær, *Int. J. Hydrogen Energy*, **36**, 9815 (2011).
5. T. E. Springer, T. A. Zawodzinski, M. S. Wilson, and S. Gottesfeld, *J. Electrochem. Soc.*, **143**, 587 (1996).
6. J. Zhang, Y. Tang, C. Song, and J. Zhang, *J. Power Sources*, **172**, 163 (2007).
7. N. H. Jalani, M. Ramani, K. Ohlsson, S. Buelte, G. Pacifico, R. Pollard, R. Staudt, and R. Datta, *J. Power Sources*, **160**, 1096 (2006).
8. I. A. Schneider, S. A. Freunberger, D. Kramer, A. Wokaun, and G. G. Scherer, *J. Electrochem. Soc.*, **154**, B383 (2007).
9. I. A. Schneider, D. Kramer, A. Wokaun, and G. G. Scherer, *Electrochem. Commun.*, **154**, B770 (2007).
10. P. Hartmann, D. Grübl, H. Sommer, J. Janek, W. G. Bessler, and P. Adelhelm, *J. Phys. Chem. C*, **118**, 1461 (2014).
11. D. Grübl, J. Janek, and W. G. Bessler, *J. Electrochem. Soc.*, **163**, A599 (2016).
12. A. M. Niroumand, W. Mérida, M. Eikerling, and M. Saif, *Electrochem. Commun.*, **12**, 122 (2010).
13. E. Engebretsen, T. J. Mason, P. R. Shearing, G. Hinds, and D. J. L. Brett, *Electrochem. Commun.*, **75**, 60 (2017).
14. A. V. Shirsath, C. Bonnet, S. Raël, and F. Lapicque, *J. Power Sources*, **531**, 231341 (2022).
15. A. V. Shirsath, C. Bonnet, D. Arora, S. Raël, and F. Lapicque, *Int. J. Heat Mass Transf.*, **190**, 122767 (2022).
16. A. V. Shirsath, S. Raël, C. Bonnet, and F. Lapicque, *Electrochim. Acta*, **363**, 137157 (2020).
17. A. V. Shirsath, S. Raël, C. Bonnet, L. Schiffer, W. G. Bessler, and F. Lapicque, *Curr. Opin. Electrochem.*, **20**, 82 (2020).
18. L. Schiffer, A. V. Shirsath, S. Raël, C. Bonnet, F. Lapicque, and W. G. Bessler, *J. Electrochem. Soc.*, **169**, 34503 (2022).
19. Q. Zhang, H. Homayouni, B. D. Gates, M. H. Eikerling, and A. M. Niroumand, *J. Electrochem. Soc.*, **169**, 44510 (2022).
20. A. Sorrentino, T. Vidakovic-Koch, R. Hanke-Rauschenbach, and K. Sundmacher, *Electrochim. Acta*, **243**, 53 (2017).
21. A. Sorrentino, T. Vidakovic-Koch, and K. Sundmacher, *J. Power Sources*, **412**, 331 (2019).
22. A. Sorrentino, K. Sundmacher, and T. Vidakovic-Koch, *Electrochim. Acta*, **390**, 138788 (2021).
23. F. Kubannek and U. Krewer, *J. Electrochem. Soc.*, **167**, 144510 (2020).
24. S. A. Vilekar and R. Datta, *J. Power Sources*, **195**, 2241 (2010).
25. C. Ziegler, T. Heilmann, and D. Gerteisen, *Electrochem. Commun.*, **155**, B349 (2008).
26. Y. Sun, T. Kadyk, A. Kulikovsky, and M. Eikerling, *J. Phys. Chem. C*, **126**, 14075 (2022).
27. A. Sorrentino, *Frequency Response Analysis Based On Concentration Inputs For The Study And Diagnosis Of Polymer Electrolyte Membrane Fuel Cells*, Otto-von-Guericke-Universitat Magdeburg, Germany (2021).
28. A. Kulikovsky, *J. Electrochem. Soc.*, **169**, 94513 (2022).